Published in final edited form as:
*ChemMedChem*. 2013 December ; 8(12): 1963–1977. doi:10.1002/cmdc.201300340.

# Probing Binding and Cellular Activity of Pyrrolidinone and Piperidinone Small Molecules Targeting the Urokinase Receptor

**Timmy Mani**[1,*], **Degang Liu**[1,*], **Donghui Zhou**[1,*], **Liwei Li**[1], **William Eric Knabe**[1], **Fang Wang**[1], **Kyungsoo Oh**[3], and **Samy O. Meroueh**[1,2,3,4]

[1]Department of Biochemistry and Molecular Biology, Indiana University School of Medicine, Indianapolis, Indiana, 46202

[2]Center for Computational Biology and Bioinformatics, Indiana University School of Medicine, Indianapolis, Indiana, 46202

[3]Department of Chemistry and Chemical Biology (IUPUI), Indiana University School of Medicine, Indianapolis, Indiana, 46202

[4]Stark Neurosciences Research Institute, Indiana University School of Medicine, Indianapolis, Indiana, 46202

## Abstract

The urokinase receptor (uPAR) is a cell-surface protein that is part of an intricate web of transient and tight protein interactions that promote cancer cell invasion and metastasis. Here we evaluate the binding and biological activity of a new class of pyrrolidinone (3) and piperidinone (4) compounds, along with derivatives of previously-identified pyrazole (1) and propylamine (2) compounds. Competition assays revealed that the compounds displaced a fluorescently-labeled peptide (AE147-FAM) with inhibition constant $K_i$ ranging from 6 to 63 μM. Structure-based computational pharmacophore analysis followed by extensive explicit-solvent molecular dynamics simulations and free energy calculations suggested pyrazole-based **1a** and piperidinone-based **4** adopt different binding modes, despite their similar two-dimensional structures. In cells, compounds **1b** and **1f** showed significant inhibition of breast MDA-MB-231 and pancreatic ductal adenocarcinoma (PDAC) cell proliferation, but **4b** exhibited no cytotoxicity even at concentrations of 100 μM. **1f** impaired MDA-MB-231 invasion, adhesion, and migration in a concentration-dependent manner, while **4b** inhibited only invasion. **1f** inhibited gelatinase (MMP-9) activity in a concentration-dependent manner, while **4b** showed no effect suggesting different mechanisms for inhibition of cell invasion. Signaling studies further highlighted these differences, showing that pyrazole compounds completely inhibited ERK phosphorylation and impaired HIF1α and NF-κB signaling, while pyrrolidinone and piperidinone (3 and **4b**) had no effect. Annexin V staining suggested that the effect of pyrazole-based **1f** on proliferation was due to cell killing through an apoptotic mechanism.

Corresponding Author: Samy Meroueh, Department of Biochemistry and Molecular Biology, Indiana University School of Medicine, 410 W. 10th Street, HITS 5000, Indianapolis, IN 46202, Tel: (317) 274-8315, Fax: (317) 278-9217, smeroueh@iupui.edu.
*authors contributed equally

## Introduction

A characteristic of malignant tumors is the ability of a small subpopulation of cells to escape from the primary tumor (1-3). Throughout the metastatic cascade and formation of new blood vessels, there is an intense process of extracellular matrix (ECM) degradation (4). With increased motility and more effective adhesion to the ECM, malignant cells eventually gain access to the vasculature and spread to distant sites to form new colonies (3). These processes require a complex interplay of various cell surface-associated proteins (4,5). Among them, the glycosyl-phosphatidylinositol (GPI) anchored urokinase receptor (uPAR) has been implicated in nearly every step of cancer metastasis including adhesion (6-8), migration (8-10), invasion (8,9,11-14), and angiogenesis (9,11,12). This is attributed to its large number of transient and tight protein-protein interactions with soluble and membrane proteins (15).

uPAR contributes to pericellular proteolysis by binding and sequestering the multi-domain protease urokinase-type plasminogen activator (uPA) to the cell surface (16,17). Most of its reported interactions are transient, such as binding to vitronectin (18), integrins (19), or receptor tyrosine kinases such as the platelet-derived growth factor receptor PDGFR (20). Indirect interactions with EGFR and LRP1 have also been reported (21-23). The former is expected to occur through integrin, while the latter is mediated by PAI-1, which eventually leads to endocytosis and the recycling of uPAR. The weak interactions have only been detected in cellular studies except for the binding of the SMB domain of vitronectin to uPAR, which has been extensively studied through biophysical studies using surface plasmon resonance (SPR) (24). A crystal structure of uPAR in complex with the amino-terminal fragment of ATF ($uPA_{ATF}$) shows the presence of a large pocket with hydrophobic characteristic that is located at the uPAR•uPA interface (25,26).

Small molecules that bind to uPAR are expected to modulate its function. We have recently reported three classes of compounds that target uPAR (8,13). An anthraquinone-based compound (IPR-803) was shown to bind at submicromolar affinity (0.2 μM) (27) and inhibited the uPAR•uPA interaction with an $IC_{50}$ of 10 μM (13). Pyrazole-based compounds displaced a fluorescently-labeled peptide with an $IC_{50}$ of 30 μM. Cellular studies of these compounds revealed inhibition of breast MDA-MB-231 adhesion, migration invasion, and angiogenesis (28). This range of cellular activity, particularly its inhibition of cell growth, suggested that the compound may likely inhibit other targets in addition to uPAR, making it a potentially useful multi-targeted agent. *In vivo*, the compound had promising pharmacokinetics and little toxicity (8).

Starting with the structure of the pyrazole- and propylamine-based compounds, we identify a series of derivatives from commercial sources that include molecules with pyrrolidinone and piperidinone core structures. Additional derivatives of the pyrazole-based compounds are designed and synthesized. The four classes of compounds were evaluated in breast MDA-MB-231 and pancreatic ductal adenocarcinoma (PDAC) PANC-1 cells and revealed distinct biological activity despite their two-dimensional structural similarity. Finally, gel zymography, immunoblotting, and flow cytometry studies were carried out to gain further insight into their mechanism of action.

## Materials and Methods

### Fluorescence polarization

Polarized fluorescence intensities were measured using EnVision® Multilabel Plate Readers (PerkinElmer) with excitation and emission wavelengths of 485 and 530 nm, respectively (8,13). Samples were prepared in black BD Falcon™ 384-well Microplate with a final volume of 50 μL in duplicates. First, the compounds were serially diluted in dimethylsulfoxide (DMSO) and further diluted in 1×PBS buffer with 0.01% Triton X-100 to make final concentrations of 100 μM to 0.046 μM. Triton X-100 was added in the buffer to avoid compound aggregation. 35 μL of the compound solution and 10 μL of PBS containing uPAR was added to the wells and incubated for at least 15 minutes to allow the compound to bind to the protein. Finally, 5 μL of fluorescently-labeled AE147 peptide AE147-FAM (K-S-D-Cha-F-s-k-Y-L-W-S-S-K; Cha: L-b-cyclohexyl-alanine) was added to make a total volume of 50 μL in each well resulting in final uPAR and peptide concentrations of 320 and 100 nM, respectively. The final DMSO concentration was 2%, which had no effect on the binding of the peptide. Controls included wells containing only the peptide and wells containing both protein and peptide each in quadruplicates to ensure the validity of the reaction assay. A unit of millipolarization (mP) was used for calculating percentage inhibition of the compounds. Inhibition constants were measured using the *K*i calculator available at http://sw16.im.med.umich.edu/software/calc_ki/.

### Reagents

Biotinylated anti-human uPAR antibody (BAF807) was purchased from R&D Systems (Minneapolis, MN). Phospho-p44/42 MAPK (Thr202/Tyr204) rabbit monoclonal antibody (4370) and p44/42 MAPK mouse monoclonal antibody (9107) were from Cell Signaling Technology, Inc. (Danvers, MA). Actin (C-2, sc-8432) antibody was from Santa Cruz Biotechnology Inc. (Santa Cruz, CA).

### Cell Culture

MDA-MB-231 and PANC-1 cells were cultured in Dulbecco's Modified Eagle Medium (Cellgro, Manassas, VA). AsPC-1 cells were cultured in RPMI-160 medium. Each medium was supplemented with 10% FBS, 1% penicillin/streptomycin and cells were cultured in a 5% $CO_2$ atmosphere at 37°C.

### Cell Viability

$10^4$ cells (MDA-MB-231, PANC-1 or AsPC-1) were plated overnight in 100 μl/well of 96 well plates. Cells were treated with DMSO (control) or compounds at the indicated concentrations for 3 days. Viable cells were quantified by MTT assay at absorbance of 570 nm and 630 nm (reference background) as previously described (8,29).

### Adhesion

96-well plates were coated with 15 ng $\mu l^{-1}$ fibronectin (Sigma-Aldrich, St. Louis, MO) at 4 °C overnight, then blocked with 2% BSA in PBS for 1 h, as described previously (8,13,30). After starving with serum-free medium for 4 h, MDA-MB-231 cells ($2.5 \times 10^4$ cells $ml^{-1}$)

were suspended in 100 μl of 0.1% FBS DMEM medium with various concentrations of uPAR compounds or DMSO control at 37 °C for 90 min. Medium was then carefully suctioned out from each well. Each well was washed three times with PBS and the number of adherent cells was quantified by MTT assay at 570 nm and 630 nm.

## Invasion

Invasion assays were performed using BD Biocoat Matrigel invasion chambers (BD Biosciences, San Jose, CA) as previously described (8,13,31). The undersurface of the inserts was coated with 30 ng $\mu l^{-1}$ of fibronectin at 4 °C overnight. The inserts were equilibrated with 0.5 mL of serum-free medium for 2 h at 37 °C. After 4 h of serum starvation, cells were harvested and $5 \times 10^4$ cells in 500 μl medium containing 0.1% FBS and the indicated compounds or 1% DMSO control were plated onto the upper chamber. 500 μL of 10% FBS medium containing the same amount of compounds or DMSO control was added to the lower chamber. After a 16 h incubation at 37°C in 5% $CO_2$, non-invaded cells were removed from the upper chamber with a cotton swab, and the invaded cells were fixed in methanol for 30 min at room temperature and stained with Hematoxylin Stain Harris Modified Method (Fisher Scientific, Waltham, MA) for 1 h at room temperature. We washed the filters with water 3 times. Filters were air-dried, and the number of invaded cells was counted in ten separate 200 × fields.

## Gelatin zymography

MDA-MB-231 cells were treated with compounds in serum free medium for 24 h (8,32,33). The conditioned medium was collected and concentrated by Amicon Ultra centrifugal filter units (Millipore, #UFC 501024), and electrophoresed on 7.5% sodium dodecyl sulfate (SDS) polyacrylamide gels containing 1 mg/mL gelatin. After electrophoresis, the gel was washed twice in 2.5% Triton X-100 for 30 min at room temperature and incubated in buffer that contained 50 mM Tris-HCl (pH 7.6), 200 mM NaCl, 10 mM $CaCl_2$, and 0.02% Brij 35 at 37 °C for 36 h. Then, the gels were stained with 0.05% Coomassie brilliant blue (CBB) and de-stained with 30% methanol in 10% acetic acid. Areas of gelatinolytic degradation appeared as transparent bands on the blue stained background of the gel. Data were quantified using Li-Cor Odyssey Imaging System (Li-Cor, Lincoln, NE).

## Western blot analysis

Six-well plates were coated with 30 ng $\mu l^{-1}$ of fibronectin at 4 °C overnight. $1.5 \times 10^6$ serum starved MDA-MB-231 cells were plated onto each well in the presence of DMSO (control) or 50 μM compounds for 30 minutes. Total cell lysates were prepared in standard RIPA extraction buffer containing protease and phosphatase inhibitors (Sigma). Thirty μg of protein was separated by 10% SDS-PAGE and transferred to nitrocellulose membranes (Amersham, Arlington Heights, IL). The membranes were immunoprobed with phospho-p44/42 MAPK (Thr202/Tyr204) rabbit monoclonal antibody (1:2000) or p44/42 MAPK mouse monoclonal antibody (1:2000) at 4°C overnight. Next, membranes were incubated with IRDye 800-conjugated goat anti-mouse IgG (Rockland) or Alexa Fluor 680 goat anti-rabbit IgG (Invitrogen) as secondary antibodies. Bands were detected using Li-Cor Odyssey Imaging System (Li-Cor, Lincoln, NE).

### Wound Healing Assay

Confluent cell monolayers in 12-well plates were wounded by scraping with a micropipette tip. The cells were washed and then cultured in complete media containing the compounds. The degree of wound closure was assessed in three randomly chosen regions by measuring the distance between the wound edges just after wounding and after 16 h and 40 h under Nikon Diaphot 300 microscope (13).

### Apoptosis Assay

MDA-MB-231 cells were treated with indicated concentrations of **1a**, **1f**, **1i**, **3** and **4** or 1% DMSO control for 24 h and flow cytometry analysis was performed as described previously (8).

### Reporter Assay

MDA-MB-231 cells were transfected with each reporter assay. 16h after carrying out the transfection, the medium was changed to complete medium (DMEM containing 10% of fetal bovine serum, 1% NEAA, 100 U/ml Penicillin and 100 μg/ml Streptomycin). After 46 h of transfection, cells were treated with **1f** at 25 μM. After 48 h of transfection, the dual-luciferase assay was used to measure the ratio of firefly versus Renilla luciferase units. The fold change was calculated by dividing the normalized luciferase ratio of each treated pathway-focused reporter by the normalized luciferase ratio of the untreated pathway-focused reporter. Experiments were performed in triplicate.

### Pharmacophore Hypotheses

Twelve of the highest affinity compounds from pyrazole, pyrrolidinone and piperidinone derivatives (four from each series) were selected to generate pharmacophore hypotheses. Compound structures were prepared with LigPrep to enumerate all possible enantiomers. Three-dimensional conformations of compounds were generated by docking compounds to the uPA binding site on multiple uPAR crystal structures. We have included uPAR crystal structures obtained from the PDB databank both in its complex form (PDB code: 1YWH, 3BT2, 3U73) and in its apo form (PDB code: 3U74). uPAR structures were prepared with Protein Preparation Wizard in the Schrodinger (Portland, OR) modeling suite by removing solvent and ligands, creating disulfide bonds, filling missing side chains, adding hydrogen atoms and optimizing hydrogen network to a pH neutral environment. The docking of compounds to uPAR was carried out using Autodock Vina (34) (version 1.1.2). All optional docking parameters were kept at default values except that the num_modes was reset from 9 to 50 and exhaustiveness from 8 to 100. The docked conformations of the compounds, whose predicted binding affinity (vina score) are stronger than -7.0 kcal/mol, were kept for hypotheses generation.

The Phase program from Schrodinger was employed to generate common pharmacophore hypotheses from docked conformations. The standard features (Acceptor, Donor, Hydrophobic, Negative, Positive, and Aromatic Rings) implemented in the Phase program were used. To find common pharmacophores, a restriction of matching all 12 compounds to a five-site pharmacophore was applied. Further restrictions were applied to match at least

two aromatic rings out of a maximum of 3 and 1 acceptor site out of a maximum of 2. After scoring the active compounds, 18 hypotheses survived with the default scoring function. Clustering on the hypotheses reduced the number down to 16. The hypotheses were then visualized in the presence of the uPAR receptor structure. Six hypotheses were selected for further evaluation.

## QSAR Model Development

A set of 30 compounds for training and another 30 for testing, whose activity was uniformly distributed from most active to in-active across three different series, were prepared for QSAR model development. With the QSAR Model Development Tools provided in the Phase program, we built atom-based QSAR models using the partial least squared (PLS) regression method applying a set of binary valued variables that encode whether or not ligand atoms occupy various cube-shaped elements of space based on the hypotheses developed above. The QSAR model performance was assessed using a number of metrics, including $R^2$ the coefficient of determination for regression, stability (model stability to the change of training set composition), $Q^2$ on the test set, and Pearson correlation r on the test set. Assuming that good pharmacophore hypotheses will generate good QSAR model performance, two pharmacophore models (HS1119 and HS1135) were selected from the hypothesis pool with the aforementioned metrics, which were further assessed with extensive molecular dynamics simulations and energy calculations.

## Molecular dynamics (MD) simulations and MM-PBSA calculations

One active compound from each of three series of the compound was selected for molecular dynamics simulations. Here we used **1a**, **3a** and **4c** to represent the three series respectively. The compound binding pose that conformed to the corresponding hypothesis was used for setting up the simulation. In total, six MD simulations were carried out on three uPAR-compound complexes in two binding modes based on hypotheses HS1119 and HS1135 respectively. The uPAR crystal structure with PDB code 1YWH was used for all the simulations. The protocol for setting up the MD simulations was described elsewhere (35). Briefly, the simulation of uPAR protein and compound complex solvated by TIP3P (36) water molecules were carried out using AMBER9 (37) MD simulation package with ff99SB (38) protein force field. A deliberate annealing process (39) was employed to equilibrate the solvated structures before production runs were carried out. The *pmemd* in AMBER was employed for production runs. By assigning different initial velocities, four independent simulation trajectories 12 ns in length were carried out for each uPAR-compound complex. The first 2 ns on each trajectory was discarded for equilibration. MD snapshots were saved every 2 ps, which results in 5,000 structures per trajectory.

The binding energy of compounds to uPAR protein was calculated with MM-PBSA approach (40). The conformational stability of the bound compound during simulations was analyzed using RMSD from its initial binding mode. In total, 600 snapshots were extracted evenly from the production trajectories that kept on the initial binding mode and subject to MM-PBSA energy analysis. The MM-PBSA Perl scripts in Amber9 were employed to determine the binding energy.

## General

All chemicals were purchased from either Aldrich or Acros and used as received. Column chromatography was carried out with silica gel (25-63 μ and used as received). $^{1}$H and $^{13}$C NMR were recorded in $CDCl_3$ or $d_4$-Methanol on a Bruker 500 MHz spectrometer. Chemical shifts are reported in ppm using either residual $CHCl_3$ or MeOH as internal references.

**1-(*tert*-butoxycarbonyl)piperidine-4-carboxylic acid (6)—**To a stirred solution of isonipecotic acid (77.4 mmol, 10.0 g) and potassium carbonate (154.8 mmol, 21.4 g) in water (150 mL) at 0 °C was added dropwise a solution of di-*t*-butyldicarbonate (77.4 mmol, 16.9 g) in THF (150 mL). The reaction mixture was gradually warmed to r.t. and stirred overnight. The solvents were evaporated and the residue was dissolved in DCM. DCM layer was washed with 1N HCl (3 × 100 mL), water, dried over sodium sulfate, and concentrated *in vacuo* to give pure **6** (13.03 g, 75%) as a white powder. $^{1}$H NMR (500 MHz, $CDCl_3$) $\delta$ 4.02 (br s, 2H), 2.85 (t, $J$ = 11.5 Hz, 2H), 2.49 (m, 1H), 1.90 (d, $J$ = 11.5 Hz, 2 H), 1.65 (m, 2H), 1.45 (s, 9H); $^{13}$C NMR (126 MHz, $CDCl_3$) $\delta$ 180.1, 154.7, 79.7, 40.7, 28.3, 27.6. HRMS *m/z* calcd for $C_{11}H_{18}NO_4$ $[M-H]^-$: 228.1241, found 228.1240.

***tert*-butyl 4-(2,2-dimethyl-4,6-dioxo-1,3-dioxane-5-carbonyl)piperidine-1-carboxylate (7)—**To a stirred soluion of **6** (56.8 mmol, 13.03 g) and DMAP (5.68 mmol, 694 mg) in DCM (10 mL) at 0 °C were added DCC (62.5 mmol, 12.9 g) and 2,2-dimethyl-1,3-dioxane-4,6-dione (62.5 mmol, 9.00 g) sequentially. The reaction mixture was gradually warmed to r.t. and stirred overnight. Reaction was filtered over filter paper and washed with DCM. The resultant orange solution was concentrated *in vacuo*. Product was not isolated.

***tert*-butyl 4-(3-ethoxy-3-oxopropanoyl)piperidine-1-carboxylate (8)—**To **7** was added abs. ethanol (200 mL) and the solution was refluxed for 48 h. The solution was concentrated *in vacuo* and purified by flash chromatography (DCM) to give **8** as a reddish oil (14.36 g, 85%). $^{1}$H NMR (500 MHz, $CDCl_3$) $\delta$ 12.09 (s, 0.14H, enol OH), 4.89 (s, 0.14H enol C-H), 4.13 (q, $J$ = 7.0 Hz, 2H), 4.10-3.96 (m, 2H), 3.42 (s, 2H), 2.81-2.67 (m, 2H), 2.62-2.52 (m, 1H), 1.85-1.71 (m, 2H), 1.55-1.43 (m, 2H), 1.39 (s, 9H), 1.21 (t, $J$ = 7.0 Hz, 3H); $^{13}$C NMR (126 MHz, $CDCl_3$) $\delta$ 204.0, 180.2 (enol), 172.7 (enol), 167.0, 154.4, 87.52, 79.51, 61.3, 48.5, 47.1, 28.2, 27.1, 13.9; $R_f$ = 0.2 (DCM). HRMS *m/z* calcd for $C_{15}H_{26}NO_5$ $[M+H]^+$: 300.1805, found 300.1808.

**(*E*)-*tert*-butyl 4-(3-ethoxy-2-(ethoxycarbonyl)acryloyl)piperidine-1-carboxylate (9)—**Under argon, **8** (47.9 mmol, 14.36 g), triethyl orthoformate (143.7 mmol, 24 mL), and acetic anhydride (95.8, 9 mL) were mixed and refluxed at 100 °C for 48 h. Low-boiling impurities were evaporated off and the crude product was purified by flash chromatography (DCM) to give **9**, as a yellowish oil (14.92 g, 88%). $^{1}$H NMR (500 MHz, $CDCl_3$) $\delta$ 7.59 (s, 0.54 H, minor), 7.52 (s, 1H, major), 4.24 (q, $J$ = 7.1 Hz, 2H), 4.21-4.09 (m, 7H), 4.08-3.92 (m, 4H), 3.09-3.01 (m, 0.58H, minor), 2.95-2.87 (m, 1H, major), 2.83-2.67 (m, 4H), 1.85-1.67 (m, 4 H), 1.58-1.47 (m, 4H), 1.41 (s, 19H), 1.37-1.26 (m, 9H), 1.23 (t, $J$ = 7.1 Hz, 6H); $^{13}$C NMR (126 MHz, $CDCl_3$) $\delta$ major isomer: 201.7, 165.7, 165.3, 162.3, 154.61,

112.6, 79.3. 72.2, 60.5, 48.0, 45.4, 28.3, 27.2, 15.2, 14.2; minor isomer: 199.6, 165.2, 154.59, 112.9, 72.7, 60.7, 28.0, 15.1, 14.1. HRMS *m/z* calcd for $C_{18}H_{30}NO_6$ $[M+H]^+$: 356.2068, found 356.2067.

***tert*-butyl 4-(1-(3,4-dimethylphenyl)-4-(ethoxycarbonyl)-1*H*-pyrazol-5-yl)piperidine-1-carboxylate (10)—**3,4-dimethylphenyl hydrazine was prepared from its HCl salt by washing with sat. sodium bicarbonate solution and extracting with DCM. DCM was removed *in vacuo*. To a stirred solution of free hydrazine (1.1 eq) in abs. ethanol (0.3 M) was added **9** (1.0 eq) in abs. ethanol (0.1 M). The reaction was refluxed at 100 °C for 48 h. Ethanol was removed *in vacuo* and the crude reddish-brown residue was purified by flash chromatography (1% MeOH/DCM) to give **10** (4.76 g, 82%) as a reddish-brown oil. $^1$H NMR (500 MHz, $CDCl_3$) $\delta$ 7.95 (s, 1H), 7.17 (d, *J* = 10.0 Hz, 1H), 7.08 (s, *J* = 10.0 Hz, 1H), 6.96 (d, *J* = 10.0 Hz, 1H), 4.25 (q, *J* = 7.1 Hz, 2H), 4.13-4.01 (m, 2H), 3.09-3.02 (m, 1H), 2.61-2.45 (m, 1H), 2.28 (s, 3H), 2.26 (s, 3H), 2.25-2.15 (m, 2H), 1.84-1.71 (m, 1H), 1.51 (app d, 2H), 1.39 (s, 9H), 1.31 (t, *J* = 7.0 Hz, 3H);

**5-(1-(*tert*-butoxycarbonyl)piperidin-4-yl)-1-(3,4-dimethylphenyl)-1*H*-pyrazole-4-carboxylic acid (11)—**To a stirred solution of **10** (1.0 eq) in 95% ethanol (0.1 M) was added a 2.0 M NaOH solution (4.0 eq). The reaction mixture was refluxed at 70 °C for 20 h. Ethanol was removed *in vacuo* and the resulting solid was acidified to pH 2 at 0 °C using 1M HCl. The reddish-brown solid was filtered off and washed with cold water to give **11** (3.57 g, 80%) as a tan solid. $^1$H NMR (500 MHz, $CDCl_3$) $\delta$ 8.06 (s, 1H), 7.29-7.22 (m, 1H), 7.12 (s, 1H), 7.03 (d, *J* = 8.0 Hz, 1H), 4.27-4.01 (m, 2H), 3.12 (app t, *J* = 12.0 Hz, 1H), 2.69-2.55 (m, 2H), 2.34 (s, 3H), 2.32 (s, 3H), 2.29-2.20 (m, 2H), 1.57-1.54 (m, 2H), 1.46 (s, 9H); $^{13}$C NMR (126 MHz, $CDCl_3$) $\delta$ 168.1, 154.9, 150.6, 143.5, 138.3, 138.1, 136.8, 130.2, 127.5, 123.6, 111.1, 79.6, 35.1, 28.5, 28.4, 19.8, 19.6. HRMS *m/z* calcd for $C_{22}H_{30}N_3O_4$ $[M+H]^+$: 400.2231, found 400.2246.

***tert*-butyl 4-(4-((3,5-dimethylphenyl)carbamoyl)-1-(4-isopropylphenyl)-1*H*-pyrazol-5-yl)piperidine-1-carboxylate – (12e-i)—**To a stirred solution of **11** (1.0 eq) and DMAP (0.1 eq) in DCM (0.1 M) at 0 °C was added DCC (1.1 eq) and aniline (1.0 eq) sequentially. The reaction was gradually warmed to r.t., and stirred for 48 h. DCM was removed in vacuo and the crude product was isolated and flash columned with 30% ethyl acetate/hexanes to remove unreacted starting material. The isolated semi-pure material was used immediately in the next step.

**1-(3,4-dimethylphenyl)-*N*-(3,5-dimethylphenyl)-5-(piperidin-4-yl)-1*H*-pyrazole-4-carboxamide - (5d-h)—**To a stirred solution of **12e-i** (1.0 eq) in DCM (0.5 M) at 0 °C was added TFA (0.5 M). The reaction mixture was warmed to r.t. and stirred for 1 h. The solvents were removed *in vacuo*. The organic residue was re-dissolved in DCM. The organic layer was washed with sat. sodium bicarbonate, brine, and dried over $MgSO_4$. The solvent was removed *in vacuo* to yield **1e-i.** (In some cases purification by flash chromatography was employed using a solvent system of 10% (10% $NH_4OH$/MeOH)/DCM).

**1-(3,4-dimethylphenyl)-*N*-(3-methoxy-5-(trifluoromethyl)phenyl)-5-(piperidin-4-yl)-1H-pyrazole-4-carboxamide - (1e)—**(42 mg, 36%); $^{1}$H NMR (500 MHz, $CDCl_3$) $\delta$ 8.26 (s, 1H), 7.98 (s, 1H), 7.46 (s, 1H), 7.41 (s, 1H), 7.22 (d, *J* = 8.0 Hz, 1H), 7.08 (m, 1H), 7.00 (d, *J* = 8.0 Hz, 1H), 6.85 (s, 1H), 4.86 (br s, 2H), 3.81 (s, 2H), 3.25 (app d, *J* = 12.5 Hz, 2H), 3.09 (m, 1H), 2.64 (app t, *J* = 11.0 Hz, 2H), 2.45 (m, 2H), 2.32 (s, 3H), 2.29 (s, 3H), 2.29 (m, 2H), 1.67 (app d, *J* = 12.5 Hz, 2H); $^{13}$C NMR (126 MHz, $CDCl_3$) $\delta$ 161.8, 160.3, 148.6, 139.8, 138.9, 138.6, 138.3, 136.6, 130.4, 127.3, 123.5, 115.1, 55.6, 45.1, 34.1, 28.2, 19.8, 19.5. HRMS *m/z* calcd for $C_{25}H_{28}F_3N_4O_2$ $[M+H]^+$: 473.2159, found 473.2145.

***N*-(2-(benzyloxy)phenyl)-1-(3,4-dimethylphenyl)-5-(piperidin-4-yl)-1*H*-pyrazole-4-carboxamide - (1f)—**(51 mg, 41%); $^{1}$H NMR (500 MHz, $CDCl_3$) $\delta$ 8.50 (d, *J* = 7.0 Hz, 1H), 8.31 (s, 1H), 7.69 (s, 1H), 7.45-7.40 (m, 4H), 7.36 (m, 1H), 7.24 (d, *J* = 8.0 Hz, 1H), 7.13 (s, 1H), 7.07-6.99 (m, 4H), 5.15 (s, 2H), 3.16-3.06 (m, 3H), 2.54 (app t, *J* = 11.0 Hz, 2H), 2.34 (s, 3H), 2.32 (s, 3H), 2.30 (m , 2H), 2.03 (br s, 1H), 1.60 (app d, *J* = 12.5 Hz, 2H); $^{13}$C NMR (126 MHz, $CDCl_3$) $\delta$ 161.5, 149.6, 147.2, 138.6, 138.1, 137.9, 137.2, 136.4, 130.1, 128.8, 128.5, 128.4, 127.6, 127.5, 123.7, 123.5, 121.6, 119.8, 115.8, 111.7, 71.1, 46.7, 35.3, 31.6, 30.6, 29.0, 22.6, 19.8, 19.6, 14.1. HRMS *m/z* calcd for $C_{30}H_{33}N_4O_2$ $[M+H]^+$: 481.2598, found 481.2596.

**1-(3,4-dimethylphenyl)-*N*-(4-fluorophenethyl)-5-(piperidin-4-yl)-1*H*-pyrazole-4-carboxamide - (1g)—**(61 mg, 58%); $^{1}$H NMR (500 MHz, $CDCl_3$) $\delta$ 7.59 (s, 1H), 7.26-7.16 (m, 3H), 7.09 (s, 1H), 7.02-6.97 (m, 3H), 5.99 (m, 1H), 3.63 (dd, *J* = 12.5, 6.5 Hz, 2H), 3.13-3.05 (m, 3H), 2.89 (t, *J* =7.0 Hz, 2H), 2.56 (app t, *J* =11.0 Hz, 2H), 2.33 (s, 3H), 2.30 (s, 3H), 2.28 (m, 2H), 1.58 (app d, *J* =12.5 Hz, 2H); $^{13}$C NMR (126 MHz, $CDCl_3$) $\delta$ 163.7, 162.6, 160.7, 148.5, 138.5, 138.1, 138.0, 137.0, 134.6, 130.2, 127.4, 123.6, 115.5, 115.3, 115.1, 46.1, 40.7, 35.0, 34.7, 30.0, 19.8, 19.5. HRMS *m/z* calcd for $C_{25}H_{30}FN_4O$ $[M+H]^+$: 421.2398, found 421.2386.

**1-(3,4-dimethylphenyl)-*N*-(4-isopropylphenyl)-5-(piperidin-4-yl)-1*H*-pyrazole-4-carboxamide - (1h)—**(60 mg, 58%); $^{1}$H NMR (500 MHz, $CDCl_3$) $\delta$ 7.87 (s, 1H), 7.82 (s, 1H), 7.23-7.17 (m, 4H), 7.11 (s, 1H), 7.04-7.02 (m, 1H), 3.12-3.05(m, 4H), 2.88 (m, 1H), 2.53 (app t, *J* = 11.0 Hz, 2H), 2.33 (s, 3H), 2.30 (s, 3H), 2.28 (m, 2H), 1.60 (app d, *J* = 12.5 Hz, 2H), 1.22 (d, *J* = 7.0 Hz, 6H); $^{13}$C NMR (126 MHz, $CDCl_3$) $\delta$ 161.9, 149.2, 145.0, 138.7, 138.1, 138.0, 137.0, 135.6, 130.1, 127.5, 126.8, 123.6, 120.6, 115.5, 46.3, 34.9, 33.5, 30.2, 24.0, 19.8, 19.5. HRMS *m/z* calcd for $C_{26}H_{33}N_4O$ $[M+H]^+$: 417.2649, found 417.2637.

**1-(3,4-dimethylphenyl)-5-(piperidin-4-yl)-*N*-(4-propylphenyl)-1*H*-pyrazole-4-carboxamide - (1i)—**(68 mg, 65%); $^{1}$H NMR (500 MHz, $CDCl_3$) $\delta$ 7.85 (s, 1H), 7.81 (s, 1H), 7.44 (m, 2H), 7.22 (d, *J* = 8.0 Hz, 1H), 7.16-7.10 (m, 3H), 7.05-7.03 (m, 1H), 3.13-3.02 (m, 3H), 2.57-2.47 (m, 4H), 2.33 (s, 3H), 2.30 (s, 3H), 2.29 (m, 2H), 1.66 (br s, 1H), 1.61-1.55 (m, 4H), 0.93 (t, *J* = 7.0 Hz, 3H); $^{13}$C NMR (126 MHz, $CDCl_3$) $\delta$ 161.9, 149.5, 138.8, 138.7, 138.0, 137.9, 137.1, 135.5, 130.1, 128.9, 127.5, 123.6, 120.4, 115.5, 46.7, 37.4, 35.2, 30.8, 24.5, 19.8, 19.5, 13.7. HRMS *m/z* calcd for $C_{26}H_{33}N_4O$ $[M+H]^+$: 417.2649, found 417.2646.

**4-methoxy-*N*-(4-methoxybenzylidene)aniline - (13)—**In a round bottom flask with *p*-anisidine (1.0 g, 8 mmol) was added dichloromethane (40 mL), anhydrous magnesium sulfate (6 g), and followed by *p*-anisaldehyde (0.97 mL, 8 mmol). The reaction was stirred for 72 h and was then filtered and the solvent was removed *in vacuo* to give 1.92 g (99%) of an off-white solid. $^1$HNMR (500 MHz, $CDCl_3$) $\delta$ 8.40 (s, 1H), 7.83 (d, *J* = 8.5 Hz, 2H), 7.21 (d, *J* = 8.5 Hz, 2 H), 6.97 (d, *J* = 9.0 Hz, 2H), 6.92 (d, *J* = 9.0 Hz, 2H), 3.86 (s, 3H), 3.83 (s, 3H).

**1,2-bis(4-methoxyphenyl)-5-oxopyrrolidine-3-carboxylic acid - (14)—**A solution of imine **13** (200 mg, 0.83 mmol) and succinic anhydride (200 mg, 0.83 mmol) in xylenes (1 mL) was refluxed for 24 h. The reaction was slowly cooled to ambient temperature and extracted with saturated sodium bicarbonate (3x). The aqueous extracts were washed with hexane and then made acidic by addition of concentrated HCl resulting in a white precipitate that was extracted into ether. The ether extract was dried and removed *in vacuo* to give a yellow-white powder (181 mg, 64%). $^1$HNMR (500 MHz, $CDCl_3$) $\delta$ 7.21 (d, *J* = 9.0 Hz, 2H), 7.16 (d, *J* = 9.0 Hz, 2H), 6.83 (d, *J* = 9.0 Hz, 2H), 6.77 (d, *J* = 9.0 Hz, 2H), 5.38 (d, *J* = 5.0 Hz, 1H), 3.76 (s, 3H), 3.72 (s, 3H), 3.20-3.14 (m, 1H), 3.05 (dd, *J* = 17.5, 9.5 Hz, 1H), 2.96 (dd, *J* = 17.5, 7.0 Hz, 1H).

***N*-(2-ethoxyphenyl)-1,2-bis(4-methoxyphenyl)-5-oxopyrrolidine-3-carboxamide - (3)—**To a stirred solution of oxo-pyrrolidine carboxylic acid **14** (181 mg, 0.53 mmol) and DMAP (6 mg, 0.053 mmol) in DCM (5 mL) at 0 °C was added DCC (120 mg, 0.58 mmol) followed by *o*-phenetidine (0.069 mL, 0.53 mmol). The reaction was warmed to ambient temperature and stirred for 3 days. The reaction was filtered over Celite and the solvent was removed *in vacuo*. The crude solid was purified by flash chromatography eluting with 60% ethyl acetate/hexane to give 146 mg (70%), as a white solid. $^1$HNMR (500 MHz, $CDCl_3$) $\delta$ 8.38 (d, *J* = 8.0 Hz, 1H), 7.58 (s, 1H), 7.21-7.15 (m, 4H), 7.06-7.01 (m, 1H), 7.00 – 6.93 (m, 1H), 6.84-6.79 (m, 3H), 6.79-6.74 (m, 2H), 5.34 (d, *J* = 7.0 Hz, 1H), 4.04-3.94 (m, 2H), 3.75 (s, 3H), 3.71 (s, 3H), 3.24-3.11 (m, 2H), 3.00-2.93 (m, 1H), 1.26 (t, *J* = 7.0 Hz, 3H); $^{13}$CNMR (126 MHz, $CDCl_3$) $\delta$ 172.3, 168.7, 159.4, 157.3, 147.0, 131.4, 130.1, 128.1, 127.1, 125.4, 124.2, 120.9, 119.9, 114.4, 114.0, 110.9, 66.6, 64.0, 55.2, 55.1, 50.3, 34.8, 14.5. HRMS *m/z* calcd for $C_{27}H_{29}N_2O_5$ $[M+H]^+$: 461.2071, found 461.2080.

**N-(4-fluorobenzylidene)-4-methoxyaniline - (15)—**In a round bottom flask with *p*-anisidine (1.0 g, 8 mmol) was added dichloromethane (40 mL), anhydrous magnesium sulfate (6 g), and followed by 4-fluorobenzaldehyde (0.86 mL, 8 mmol). The reaction was stirred for 72 h and was then filtered and the solvent was removed *in vacuo* to give 1.91 g (99%) of an off-white solid. $^1$HNMR (500 MHz, $CDCl_3$) $\delta$ 8.44 (s, 1H), 7.88 (dd, *J* = 8.5, 5.5 Hz, 2H), 7.23 (d, *J* = 8.5 Hz, 2H), 7.15 (t, *J* = 9.0 Hz, 2H), 6.94 (d, *J* = 9.0 Hz, 2H), 3.84 (s, 3H).

***anti*-2-(4-fluorophenyl)-1-(4-methoxyphenyl)-6-oxopiperidine-3-carboxylic acid - (16)—**A solution of imine **15** (910 mg, 3.97 mmol) and glutaric anhydride (453 mg, 3.97 mmol) in xylenes (5 mL) was refluxed for 72 h. The reaction was slowly cooled to ambient temperature and extracted with saturated sodium bicarbonate (3x). The aqueous extracts

were washed with hexane and then made acidic by addition of concentrated HCl resulting in a white precipitate (457 mg, 34%). $^1$HNMR (500 MHz, $CDCl_3$) $\delta$ 7.23-7.19 (m, 2H), 7.07 (d, *J* = 9.0 Hz, 2H), 7.01-6.96 (m, 2H), 6.74 (d, *J*= 9.0 Hz, 2H), 5.37 (d, *J* = 3.5 Hz, 1H), 3.70 (s, 3H), 2.84 (q, *J* = 9.5, 4.5 Hz, 1H), 2.78-2.64 (m, 2H), 2.40 (t, *J* = 7.0 Hz, 1H), 2.36 (t, *J* = 7.0 Hz, 1H), 2.23-2.16 (m , 1H), 2.10-2.00 (m, 1H).

***anti*-N-(2,4-dimethoxyphenyl)-2-(4-fluorophenyl)-1-(4-methoxyphenyl)-6-oxopiperidine-3-carboxamide - (4)—**To a stirred solution of oxo-pyrrolidine carboxylic acid **16** (457 mg, 1.33 mmol), EDC (255 mg, 1.33 mmol), and HOBT (54 mg, 0.40 mmol) in DCM (7 mL) at 0 °C was added dropwise 2, 4-dimethoxyaniline (0.189 mL, 1.33 mmol). The reaction was warmed to ambient temperature and stirred for 2 days. The mixture was evaporated and partitioned between 1M HCl and ethyl acetate. The organic layer was washed with saturated sodium bicarbonate, brine, dried over anhydrous sodium sulfate, and evaporated. The crude solid was purified by flash chromatography eluting with ethyl acetate to give 444 mg (70%) of a pinkish solid after trituration with hexanes. $^1$HNMR (500 MHz, $CDCl_3$) $\delta$ 8.10 (d, *J* = 9.0 Hz, 1H), 7.30 (s, 1H), 7.21-7.15 (m, 2H), 7.02 (d, *J* = 9.0 Hz, 2H), 6.93 (t, *J* = 9.0 Hz, 2H), 6.73 (d, *J* = 9.0 Hz, 2H), 6.45 (d, *J* = 9.0 Hz, 1H), 6.40 (d, *J* = 2.5 Hz, 1H), 5.26 (d, *J* = 7.5 Hz, 1H), 3.77 (s, 3H), 3.73 (s, 3H), 3.70 (s, 3H), 2.90-2.71 (m, 3H), 2.40-2.04 (m, 2H); $^{13}$CNMR (126 MHz, $CDCl_3$) $\delta$ 169.9, 168.9, 161.1, 158.0, 156.8, 149.3, 136.0, 133.9, 129.1, 129.0, 128.9, 121.02, 120.3, 115.7, 115.5, 114.1, 103.7, 98.5, 66.1, 55.6, 55.5, 55.2, 51.1, 31.5, 31.2, 23.2, 22.6, 14.1. HRMS *m/z* calcd for $C_{27}H_{28}FN_2O_5$ $[M+H]^+$: 479.1977, found 479.1987.

## Results

### Synthesis

The synthesis of N-1 substituted pyrazoles **1e-i** (Scheme 2) followed the route reported previously (41). The pyrazole core was prepared by condensation of 1,3-dicarbonyl enol ethers with hydrazines. Thus, commercially available isonipecotic acid was protected to the N-Boc version **6**, which was converted to known β-keto ester **8** through a simple two-step sequence (coupling of Meldrum's acid followed by ethanolysis) (42). With the requisite β-keto ester **8** in hand, the formation of the pyrazole core was explored with commercially available hydrazine. Subsequent hydrolysis of **10**, the amide bond formation of **12** with various anilines, and following the removal of N-Boc gave the desired N-1 substituted pyrazoles **1e-i.**

The synthesis of substituted pyrrolidin-2-one **3** and piperidin-2-one **4** are summarized in Schemes 3 and 4, respectively. First, Schiff bases **13** and **15** were obtained with the appropriate aldehyde and amine in the presence of anhydrous $MgSO_4$ (43). The subsequent condensation of Schiff base with succinic anhydride or glutaric anhydride in refluxing xylenes gave the pyrrolidin-2-one **14** and piperidin-2-one **16** carboxylic acids, respectively (44). Amide formation was carried out by EDC coupling in the case of **16** and DCC coupling for **14** to give the final substituted pyrrolidin-2-one **3** and piperidin-2-one **4**.

## uPAR binding activity

Previously, we had reported the use of virtual screening to identify compounds that bind to uPAR (8). Docking of 300,000 compounds to the uPAR crystal structure was focused to a pocket located at the interface of the protein-protein complex between uPAR and its serine protease ligand urokinase-type plasminogen activator (uPA). Among the active compounds that had emerged were pyrazole **1** (IPR-69) and propylamine **2**. Among the top ranking candidates, two compounds shared structural similarity to **1**. These include pyrrolidinone **3** and piperidinone **4** (Scheme 1). Here, for the first time, we characterize the binding and cellular activity of these compounds along with their derivatives.

A similarity search of the ZINC chemical library was carried out using the chemical structure **1**-**4**. Derivatives were acquired and tested for activity at an initial concentration of 50 μM using a fluorescence polarization (FP) assay (Fig. 1A). The FP assay probe consisted of labeling an α-helical peptide (AE147) with fluorescein (AE147-FAM). The labeled-peptide was shown to bind to uPAR with a $K_D$ of 499 nM. A concentration-dependent study was performed for several derivatives that were active (Fig. 1B). The structure of these derivatives is shown in Tables 1-4. For **1**, four derivatives were selected, namely **1a**, **1b**, **1c**, and **1d** (Table 1). Their $K_i$ ranged from 10 to 27 μM. The replacement of the *para*-isopropopyl group of the parent compound with a dimethyl substituted phenyl ring in **1a** and **1b** enhanced the affinity of the compound from the parent compound suggesting a better fit into the binding pockets of uPAR. This is reflected in **1c** and **1d** whereby a hydrogen or a chlorine at the *meta*-position of $R_3$, also led to inhibition constants that were higher than the parent compound **1**. Starting with the structure of **1a**, a structure-based approach was followed to design and synthesize additional derivatives (**1f**-**1i**). Four compounds were more active than the parent at single concentration and were studied in a concentration-dependent manner (Table 1). The highest affinity derivative was **1e** ($K_i$ = 17 μM), whereas the lowest affinity derivative was **1g** ($K_i$ = 63.3 μM) (Table 1).

The process was repeated for compounds **2**-**4**. Similarity search identified derivatives that were tested at a single concentration and follow-up studies in a concentration-dependent manner were done for compounds that were more active than the parent. Three derivatives were identified for **2**, namely **2a**, **2b**, and **2c**, which had inhibition constants of 19.3, 33.8, and 13.9 μM respectively (Table 2). For **3**, two compounds were identified with higher affinity, namely **3a** and **3b** having $K_i$ values of 10.3 and 11.4 μM respectively (Table 3). For **4**, we found seven active derivatives with binding affinities ranging from 5.7 to 24.1 μM. The highest affinity compound was **4c**, which has a phenyl rather than a benzyl moiety at $R_3$. When two methoxy groups are introduced at $R_2$ to generate **4b**, the affinity is significantly reduced. A methoxy group at the *meta*-position is responsible for the reduced affinity since **4e** and **4f** have a methoxy moiety at the *ortho* and *para* positions with $K_i$ values that are less than 16 and 12.6 μM, respectively (Table 4).

## Computational studies

Two binding modes were selected from the pharmacophore and QSAR modeling studies (Fig. 2A and 2B). We refer to these two modes as hypothesis (HS1119) and hypothesis (HS1135). In HS1119, the $R_2$ group of the pyrazole-, piperidinone-, and pyrrolidinone

compounds are ensconced in a pocket in the uPA-binding hydrophobic pocket on uPAR (Fig. 2C). In HS1135, the $R_2$ is instead directed away from the protein toward the solvent (Fig. 2D). Rigorous computational studies were conducted to determine the stability and binding strength of the compounds in both binding modes. Explicit-solvent MD simulations for each binding mode were carried out for three compounds, **1b**, **3a**, and **4c**. Analysis of the 12 ns trajectories revealed that **1b** was highly unstable in binding mode HS1119 as evidenced by the RMSD of the compound that increases to 4 Å for three of the 12 ns trajectories and 8 Å for one of the trajectories (Fig. 3A and 3C). The compound was more stable in binding mode HS1135 (Fig. 3B and 3D). **3a** on the other hand, showed significantly greater stability in the HS1119 binding pose with an RMSD that remained within 3 Å (Fig. 3E and 3G) in contrast to the HS1135 binding pose that exhibited an RMSD greater than 6 Å for two of the trajectories (Fig. 3F and 3H). A similar observation was made for piperidinone-based **4c**, which remained remarkably stable over the course of the simulations, showing RMSDs within 1.5 Å for binding pose HS1119 (Fig. 3I and 3K) compared to the significantly larger RMSDs observed for HS1135 (Fig. 3J and 3L).

Free energy calculations using protein-compound structures collected from the MD simulations were carried out using the MM-PBSA approach (Table 5). The MM-PBSA free energy $\Delta G_{PBSA}$ is obtained by subtracting the free energy of the protein-compound complex from protein and compound for each snapshot collected from the MD simulation. The free energy consists of an internal energy term consisting of van der Waals and Coulomb potential energy ($\Delta E_{PBELE}$), a solvation energy term consists of electrostatic and non-polar components ($\Delta E_{PBTOT}$), and finally an entropy term ($T\Delta S_{NM}$) (Table 1). For **1a**, $\Delta G_{PBSA}$ was only determined only for HS1135, as the compound was unstable in the HS1119 binding mode. In contrast, piperidinone- and pyrrolidinone-based **3a** and **4c** trajectories were stable in the HS1119 binding mode and resulted in $\Delta G_{PBSA}$ of -20 and -25 kcal/mol, respectively. The trajectories for HS1135 binding mode resulted in binding less stable $\Delta G_{PBSA}$, namely -13, -11, and -21 kcal/mol for **1a**, **3a** and **4c**, respectively. The binding free energy for **3a** and **4c** was significantly more stable for the HS1119 binding mode, in contrast to the pyrazole-based **1a**, which prefers the HS1135 binding mode.

## Effect of compounds on cell proliferation

We tested the cytotoxicity of several compounds using MTT as previously described (8,29). A concentration-dependent MTT study in MDA-MB-231 cells gave $IC_{50}$ values of 31, 13, and 25 μM for **1b**, **2c**, and **1f**, respectively (Fig. 4). **1f** had $IC_{50}$ values of 14 and 22 μM in AsPC-1 and PANC-1 cell lines respectively. In comparison, **4b** showed no cytotoxicity with 70% cell viability even at 100 μM (Fig. 4).

To get insight into the cell killing mechanism, a flow cytometry analysis was performed with Annexin V-FITC and PI staining for **1a**, **1f**, **1i**, **3**, and **4** (Table 6 and Fig. 5). The level of apoptosis and necrosis in MDA-MB-231 cells was assessed after exposure to increasing concentrations of compound for 24 hours as a percentage of Annexin V-positive/PI-negative cells (apoptotic) and Annexin V-positive/PI-positive cells (necrotic) respectively (Table 5 and Fig. 5). The data reveal that only the pyrazole compounds cause apoptosis, with **1f** and **1i** exhibiting the most pronounced effects. Control DMSO-treated cells showed about 3%

apoptotic and 6% necrotic cells. At concentrations of 1, 10, 25 and 50 μM, **1f** resulted in 3, 45, 76 and 61% apoptotic cells and 7, 15, 8 and 21% necrotic cells respectively (Fig. 5F). For compound **1i**, 10, 25 and 50 μM resulted in 11, 6, 46, and 86% apoptotic cells, and 7, 9, 10, and 12% necrotic cells, respectively. Finally, **1a** exhibited less significant apoptosis with nearly 39 and 32% of cells undergoing apoptosis and necrosis at 50 μM, respectively.

Western blot analysis was performed test for the effects of compounds on MAPK signaling, given that the pathway regulates cell proliferation and survival. Western blot analysis was carried out following plating of serum starved cells onto fibronectin coated culture plates for 30 min in the presence of 50 μM compounds. Results show that pyrazole-based **1f**, **1i** and **1a** significantly impaired p44/42 MAPK phosphorylation. Propylamine-based **2c** exhibited moderate inhibition. In contrast, **4**, **4b** and **3** showed no inhibition of p44/42 MAPK phosphorylation (Fig. 6A), consistent with their complete lack of cytotoxicity. Luciferase reporter assays on MDA-MB-231 cells revealed that NF-κB, HIF1α and ERK were active even at basal level (Fig. 6B). **1f** impaired all three pathways. The effect on HIF1α is consistent with inhibition of ERK1/2 phosphorylation, which is known to control activity of HIF1α. The effect on NF-κB can also be attributed to inhibition of ERK phosphorylation. In both cases, however, it is possible that the effects are ERK-independent.

## Effect on cell invasion, migration and adhesion

To test the effects of compounds on MDA-MB-231 invasion, the Matrigel coated Boyden chamber was used as previously described (13) (Fig. 7). The compounds were initially tested at two concentrations (Fig. 7A). First, at 10 μM concentration, **1b**, **1f**, **2b**, and **2c**, and **4b**. Each compound inhibited invasion with the pyrazole (1) and propylamine (2) derivatives exhibiting highest activity, while the piperidinone (4) and pyrolidinone (3) showing milder effects. At 25 μM **1f**, **2b** and **2c** completely inhibited invasion, while compounds **1b**, **4b** and **3** showed moderate inhibition of invasion (Fig. 7A). The effects of these compounds on migration were also tested at 25 μM using wound healing. Compounds **1f** and **2c** inhibited cell migration by 70 and 50%, respectively (Fig. 7C and 7D). In contrast, **1b**, **3**, and **4b** had no effect on migration (Fig. 7C and 7D). Cell viability was studied using MTT at 16 h within a similar time frame of the invasion and migration studies (Fig. 7C). At 10 μM, most compounds did not exhibit any cytotoxicity except for **1f**, **2b** and **2c**, inhibit cell growth by 20, 60 and 80%, respectively. Hence, the effects of invasion observed at 10 μM for **1b**, **1f**, **3**, and **4b** are unlikely due to cell toxicity. At 25 μM, only the pyrrolidinone **3** and piperidone **4b** were not cytotoxic, confirming that the 50% inhibition of cell invasion at this concentration is unlikely due to effects on cell viability.

We used a Matrigel-coated Boyden chamber apparatus in a concentration-dependent study to determine the effect of **1f** and **4b** on MDA-MB-231 invasion in a concentration-dependent manner. **1f** inhibited invasion in a concentration-dependent manner with an estimated $IC_{50}$ less than 10 μM (Fig. 8A). At 25 μM, a complete inhibition of invasion was observed. To test whether the inhibition of invasion by **1f** is dependent on the degradation of ECM by matrix metalloproteinases (MMPs), we performed gelatin zymography as previously described (13,29). **1f** inhibits MMP-9 activity in a concentration-dependent manner with an $IC_{50}$ of 28 μM (Fig. 8B). Similarly at 25 μM, a complete inhibition of

migration is observed with **1f** as assessed by wound healing (Fig. 7B). We then tested the effects of the piperidinone derivative **4b** in cancer cell invasion and metastasis. Similar to pyrazole-based compound **1f** the piperidinone-based **4b** impaired invasion in a concentration-dependent manner, with 50% inhibition observed at 25 μM (Fig. 7A). Importantly **4b** showed no cytotoxicity in cell viability studies conducted in parallel with invasion studies. Furthermore, unlike **1f**, **4b** showed no inhibition of MMP-9 activity (Fig. 8B) suggesting that the effects of **4b** on invasion are MMP-9 independent.

Next, we tested the effect of the **1f** on the integrin-mediated process of cell adhesion (18,46-48). MDA-MB-231 cells were added to wells pre-coated with fibronectin. In the presence of **1f**, a concentration-dependent impairment of cell adhesion is observed with an estimated $IC_{50}$ of 25 μM (Fig. 8C). In contrast to the pyrazole-based compound **1f**, the piperidinone derivative **4b** showed no impairment of cell adhesion (Fig. 8C) consistent on the lack of effect on migration (Fig. 7B).

## Discussion

Previously, we had reported the discovery of anthraquinone-based compound (13,32,49) and pyrazole-based compound (8) that bind to uPAR and characterized their activity both *in vitro* and *in vivo*. In this study, we report the design, synthesis and biological characterization of a series of derivatives of the pyrazole-based **1**, piperidinone **4** and pyrrolidinone **3** cores that were shown to bind to uPAR. Using fluorescence polarization (FP), we measured the inhibition constants of these derivatives and their $K_i$ ranged from 6 to 63 μM. Computational studies revealed that the flat aromatic ring of the pyrazole-based compounds preferred a different binding mode to uPAR in comparison to 3 and 4. The chiral centers in the latter compounds direct the substituents bound to the central core into different pockets, resulting in better complementarity with the protein.

The difference in the structure of **1** and **4** is reflected in their dramatically different cellular activity. In cell-based assays the pyrazole-containing compound such as **1f** showed significantly greater cytotoxicity. Flow cytometry analysis revealed that this compound also caused significant apoptosis in MDA-MB-231 cells. In contrast, the piperidinone compound, **4b** was not cytotoxic even up to 100 μM. Furthermore, **1f** impaired MDA-MB-231 cell invasion, adhesion, and migration in a concentration-dependent manner, whereas **4b** inhibited invasion but had no effect on adhesion or migration. The effects of **1f** on adhesion and migration suggest that the pyrazole-based **1f** likely inhibits the interactions of uPAR with integrins. On the other hand, the lack of effects of the piperidinone compound on cell migration and adhesion suggest that it is unlikely to perturb the uPAR-integrin association. Gelatin zymography shows that **1f** impaired gelatinase (MMP-9) activity in a concentration-dependent manner, whereas the piperidinone derivative did not, indicating that these compounds also differ in their anti-invasion mechanism. It is well documented that binding of uPA to uPAR is critical for its activation, and this triggers the proteolytic degradation of the ECM (50,51). Activated uPA converts the extracellular zymogen plasminogen into the active serine protease plasmin, which degrades the ECM components including fibrinogen, fibronectin and vitronectin and activates several matrix metalloproteases (MMPs) (52-55).

Finally, our signaling studies revealed that the pyrazole-based compounds such as **1f**, **1i** and **1a** significantly inhibit MAPK signaling whereas the piperidinone compounds (4 and **4b**) and the pyrrolidinone (3) had no effect. The inhibition of MAPK phosphorylation may explain the broad cellular activity exhibited by **1f** that includes inhibition of cell growth, migration, invasion and adhesion, as well as apoptosis. The compound also impaired HIF1 α and NF-κB signaling. These effects may be due to additional unknown off-targets. Future studies will utilize these compounds as valuable leads to design derivatives with higher affinity and to unravel the protein-protein interactions of uPAR.

## Supplementary Material

Refer to Web version on PubMed Central for supplementary material.

## Acknowledgments

This research was supported by the US National Institutes of Health (NIH) (CA135380> to S.O.M.), an Indiana Genomics Initiative (INGEN) Grant from Lilly Endowment, Inc. (S.O.M.), the Indiana University Melvin and Bren Simon Cancer Center Translational Research Acceleration Collaboration (ITRAC) (S.O.M.), the Showalter Trust (S.O.M.), the Indiana University Biomedical Research Fund (S.O.M.), and a Research Scholar Grant from the American Cancer Society (RSG-12-092-01 to S.O.M.).

## References

1. Hanahan D, Weinberg RA. Hallmarks of cancer: the next generation. Cell. 2011; 144:646–674. [PubMed: 21376230]
2. Duffy MJ, McGowan PM, Gallagher WM. Cancer invasion and metastasis: changing views. Journal of Pathology. 2008; 214:283–293. [PubMed: 18095256]
3. Talmadge JE, Fidler IJ. AACR centennial series: the biology of cancer metastasis: historical perspective. Cancer Res. 2010; 70:5649–5669. [PubMed: 20610625]
4. Cairns RA, Khokha R, Hill RP. Molecular mechanisms of tumor invasion and metastasis: an integrated view. Curr Mol Med. 2003; 3:659–671. [PubMed: 14601640]
5. Woodhouse EC, Chuaqui RF, Liotta LA. General mechanisms of metastasis. Cancer. 1997; 80:1529–1537. [PubMed: 9362419]
6. De Bock CE, Lin Z, Mekkawy AH, Byrne JA, Wang Y. Interaction between urokinase receptor and heat shock protein MRJ enhances cell adhesion. Int J Oncol. 2010; 36:1155–1163. [PubMed: 20372789]
7. van der Pluijm G, Sijmons B, Vloedgraven H, van der Bent C, Drijfhout JW, Verheijen J, Quax P, Karperien M, Papapoulos S, Lowik C. Urokinase-receptor/integrin complexes are functionally involved in adhesion and progression of human breast cancer in vivo. Am J Pathol. 2001; 159:971–982. [PubMed: 11549590]
8. Wang F, Li J, Sinn AL, Knabe WE, Khanna M, Jo I, Silver JM, Oh K, Li L, Sandusky GE. Virtual Screening Targeting the Urokinase Receptor, Biochemical and Cell-Based Studies, Synthesis, Pharmacokinetic Characterization, and Effect on Breast Tumor Metastasis. J Med Chem. 2011; 54:7193–7205. [PubMed: 21851064]
9. Raghu H, Sodadasu PK, Malla RR, Gondi CS, Estes N, Rao JS. Localization of uPAR and MMP-9 in lipid rafts is critical for migration, invasion and angiogenesis in human breast cancer cells. BMC Cancer. 2010; 10:647. [PubMed: 21106094]
10. Ahmad A, Kong D, Wang Z, Sarkar SH, Banerjee S, Sarkar FH. Down-regulation of uPA and uPAR by 3,3'-diindolylmethane contributes to the inhibition of cell growth and migration of breast cancer cells. J Cell Biochem. 2009; 108:916–925. [PubMed: 19693769]
11. Kunigal S, Lakka SS, Gondi CS, Estes N, Rao JS. RNAi-mediated downregulation of urokinase plasminogen activator receptor and matrix metalloprotease-9 in human breast cancer cells results

in decreased tumor invasion, angiogenesis and growth. International journal of cancer. 2007; 121:2307–2316.

12. Subramanian R, Gondi CS, Lakka SS, Jutla A, Rao JS. siRNA-mediated simultaneous downregulation of uPA and its receptor inhibits angiogenesis and invasiveness triggering apoptosis in breast cancer cells. International Journal of Oncology. 2006; 28:831–839. [PubMed: 16525631]
13. Khanna M, Wang F, Jo I, Knabe WE, Wilson SM, Li L, Bum-Erdene K, Li J, G WS, Khanna R, Meroueh SO. Targeting multiple conformations leads to small molecule inhibitors of the uPAR.uPA protein-protein interaction that block cancer cell invasion. ACS chemical biology. 2011; 6:1232–1243. [PubMed: 21875078]
14. Xing RH, Rabbani SA. Overexpression of urokinase receptor in breast cancer cells results in increased tumor invasion, growth and metastasis. Int J Cancer. 1996; 67:423–429. [PubMed: 8707419]
15. Eden G, Archinti M, Furlan F, Murphy R, Degryse B. The urokinase receptor interactome. Curr Pharm Des. 2011; 17:1874–1889. [PubMed: 21711237]
16. Cubellis MV, Nolli ML, Cassani G, Blasi F. Binding of single-chain prourokinase to the urokinase receptor of human U937 cells. J Biol Chem. 1986; 261:15819–15822. [PubMed: 3023326]
17. Blasi F, Vassalli JD, Dano K. Urokinase-type plasminogen activator: proenzyme, receptor, and inhibitors. J Cell Biol. 1987; 104:801–804. [PubMed: 3031083]
18. Gardsvoll H, Ploug M. Mapping of the vitronectin-binding site on the urokinase receptor - Involvement of a coherent receptor interface consisting of residues from both domain I and the flanking interdomain linker region. Journal of Biological Chemistry. 2007; 282:13561–13572. [PubMed: 17355965]
19. Wei Y, Czekay RP, Robillard L, Kugler MC, Zhang F, Kim KK, Xiong JP, Humphries MJ, Chapman HA. Regulation of alpha5beta1 integrin conformation and function by urokinase receptor binding. J Cell Biol. 2005; 168:501–511. [PubMed: 15684035]
20. Kiyan J, Kiyan R, Haller H, Dumler I. Urokinase-induced signaling in human vascular smooth muscle cells is mediated by PDGFR-beta. Embo J. 2005; 24:1787–1797. [PubMed: 15889147]
21. Liu D, Aguirre Ghiso J, Estrada Y, Ossowski L. EGFR is a transducer of the urokinase receptor initiated signal that is required for *in vivo* growth of a human carcinoma. Cancer cell. 2002; 1:445–457. [PubMed: 12124174]
22. Jo M, Thomas KS, Wu L, Gonias SL. Soluble urokinase-type plasminogen activator receptor inhibits cancer cell growth and invasion by direct urokinase-independent effects on cell signaling. The Journal of biological chemistry. 2003; 278:46692–46698. [PubMed: 12963722]
23. Czekay RP, Kuemmel TA, Orlando RA, Farquhar MG. Direct binding of occupied urokinase receptor (uPAR) to LDL receptor-related protein is required for endocytosis of uPAR and regulation of cell surface urokinase activity. Molecular biology of the cell. 2001; 12:1467–1479. [PubMed: 11359936]
24. Mertens HD, Kjaergaard M, Mysling S, Gardsvoll H, Jorgensen TJ, Svergun DI, Ploug M. A flexible multidomain structure drives the function of the urokinase-type plasminogen activator receptor (uPAR). The Journal of biological chemistry. 2012
25. Huai Q, Zhou A, Lin L, Mazar AP, Parry GC, Callahan J, Shaw DE, Furie B, Furie BC, Huang M. Crystal structures of two human vitronectin, urokinase and urokinase receptor complexes. Nat Struct Mol Biol. 2008; 15:422–423. [PubMed: 18376415]
26. Huai Q, Mazar AP, Kuo A, Parry GC, Shaw DE, Callahan J, Li Y, Yuan C, Bian C, Chen L. Structure of human urokinase plasminogen activator in complex with its receptor. Science Signalling. 2006; 311:656.
27. Mani T, Wang F, Knabe WE, Sinn AL, Khanna M, Jo I, Sandusky GE, Sledge GW Jr, Jones DR, Khanna R, Pollok KE, Meroueh SO. Small-molecule inhibition of the uPAR.uPA interaction: Synthesis, biochemical, cellular, in vivo pharmacokinetics and efficacy studies in breast cancer metastasis. Bioorg Med Chem. 2013
28. Wang F, Li J, Sinn AL, Knabe WE, Khanna M, Jo I, Silver JM, Oh K, Li L, Sandusky GE, Sledge GW, Nakshatri H, Jones DR, Pollok KE, Meroueh SO. Virtual screening targeting the urokinase

receptor, biochemical and cell-based studies, synthesis, pharmacokinetic characterization, and effect on breast tumor metastasis. J Med Chem. 2011; 54:7193–7205. [PubMed: 21851064]

29. Twentyman PR, Luscombe M. A study of some variables in a tetrazolium dye (MTT) based assay for cell growth and chemosensitivity. Br J Cancer. 1987; 56:279–285. [PubMed: 3663476]
30. Wei Y, Eble JA, Wang Z, Kreidberg JA, Chapman HA. Urokinase receptors promote beta1 integrin function through interactions with integrin alpha3beta1. Molecular biology of the cell. 2001; 12:2975–2986. [PubMed: 11598185]
31. Albini A, Iwamoto Y, Kleinman HK, Martin GR, Aaronson SA, Kozlowski JM, McEwan RN. A rapid in vitro assay for quantitating the invasive potential of tumor cells. Cancer Res. 1987; 47:3239–3245. [PubMed: 2438036]
32. Wang F, Eric Knabe W, Li L, Jo I, Mani T, Roehm H, Oh K, Li J, Khanna M, Meroueh SO. Design, synthesis, biochemical studies, cellular characterization, and structure-based computational studies of small molecules targeting the urokinase receptor. Bioorg Med Chem. 2012; 20:4760–4773. [PubMed: 22771232]
33. Toth M, Fridman R. Assessment of Gelatinases (MMP-2 and MMP-9 by Gelatin Zymography. Methods Mol Med. 2001; 57:163–174. [PubMed: 21340898]
34. Trott O, Olson AJ. Software News and Update AutoDock Vina: Improving the Speed and Accuracy of Docking with a New Scoring Function, Efficient Optimization, and Multithreading. Journal of Computational Chemistry. 2010; 31:455–461. [PubMed: 19499576]
35. Li L, Uversky VN, Dunker AK, Meroueh SO. Computational Investigation of Allostery in the Catabolite Activator Protein. J Am Chem Soc. 2007 In press.
36. Jorgensen, William L.; C, J.; Madura, Jeffry D.; Impey, Roger W.; Klein, Michael L. Comparison of simple potential functions for simulating liquid water. The Journal of Chemical Physics. 1983; 79:10.
37. Case, DA.; T, AD.; Cheatham, TE., III; Simmerling, CL.; Wang, J.; Duke, RE.; Luo, R.; Merz, KM.; Wang, B.; Pearlman, DA.; Crowley, M.; Brozell, S.; Tsui, V.; Gohlke, H.; Mongan, J.; Hornak, V.; Cui, G.; Beroza, P.; Schafmeister, C.; Caldwell, JW.; Ross, WS.; Kollman, PA. AMBER 8. University of California; San Francisco: 2004.
38. Hornak V, Abel R, Okur A, Strockbine B, Roitberg A, Simmerling C. Comparison of multiple amber force fields and development of improved protein backbone parameters. Proteins-Structure Function and Bioinformatics. 2006; 65:712–725.
39. Li L, Uversky VN, Dunker AK, Meroueh SO. A computational investigation of allostery in the catabolite activator protein. Journal of the American Chemical Society. 2007; 129:15668–15676. [PubMed: 18041838]
40. Massova I, Kollman PA. Combined molecular mechanical and continuum solvent approach (MM-PBSA/GBSA) to predict ligand binding. Perspectives in Drug Discovery and Design. 2000; 18:113–135.
41. Wang AX, Xie Q, Lane B, Mollison KW, Hsieh GC, Marsh K, Sheets MP, Luly JR, Coghlan MJ. Synthesis and immunosuppressant activity of pyrazole carboxamides. Bioorg Med Chem Lett. 1998; 8:2787–2792. [PubMed: 9873623]
42. Bashford KE, Burton MB, Cameron S, Cooper AL, Hogg RD, Kane PD, MacManus DA, Matrunola CA, Moody CJ, Robertson AAB, Warne MR. The Bohlmann-Rahtz route to functionalised pyridine scaffolds and their use in library synthesis. Tetrahedron Lett. 2003; 44:1627–1629.
43. Hegedus LS, M M, Schultze LM, Yijun C, Anderson OP. J Am Chem Soc. 1984; 106:2680–2687.
44. Larson, SPJ.; Van Huis, C. Oxazolidinones as Cholesterol Absorption Inhibitors. Pfizer Products Inc; WO 2008/104875 A1
45. Li L, Uversky VN, Dunker AK, Meroueh SO. A computational investigation of allostery in the catabolite activator protein. J Am Chem Soc. 2007; 129:15668–15676. [PubMed: 18041838]
46. Gardsvoll H, Jacobsen B, Kriegbaum MC, Behrendt N, Engelholm L, Ostergaard S, Ploug M. Conformational regulation of urokinase receptor function: impact of receptor occupancy and epitope-mapped monoclonal antibodies on lamellipodia induction. The Journal of biological chemistry. 2011; 286:33544–33556. [PubMed: 21799009]

47. Gardsvoll H, Kjaergaard M, Jacobsen B, Kriegbaum MC, Huang M, Ploug M. Mimicry of the regulatory role of urokinase in lamellipodia formation by introduction of a non-native interdomain disulfide bond in its receptor. The Journal of biological chemistry. 2011; 286:43515–43526. [PubMed: 22025616]
48. Xu X, Gardsvoll H, Yuan C, Lin L, Ploug M, Huang M. Crystal structure of the urokinase receptor in a ligand-free form. Journal of molecular biology. 2012; 416:629–641. [PubMed: 22285761]
49. Mani T, Wang F, Knabe WE, Sinn AL, Khanna A, Jo I, Li J, Silver JM, Sandusky G, Sledge CB, Jones DR, Khanna R, Pollock KE, Meroueh SO. Small-molecule inhibition of the uPARuPA interaction: Synthesis, biochemical, cellular, in vivo pharmacokinetics and efficacy studies in breast cancer metastasis. Bioorg Med Chem. 2013 In press.
50. Ellis V, Scully MF, Kakkar VV. Plasminogen activation initiated by single-chain urokinase-type plasminogen activator. Potentiation by U937 monocytes. The Journal of biological chemistry. 1989; 264:2185–2188. [PubMed: 2521625]
51. Ellis V, Behrendt N, Dano K. Plasminogen activation by receptor-bound urokinase. A kinetic study with both cell-associated and isolated receptor. The Journal of biological chemistry. 1991; 266:12752–12758. [PubMed: 1829461]
52. Dano K, Andreasen PA, Grondahl-Hansen J, Kristensen P, Nielsen LS, Skriver L. Plasminogen activators, tissue degradation, and cancer. Advances in cancer research. 1985; 44:139–266. [PubMed: 2930999]
53. Castellino FJ, Ploplis VA. Structure and function of the plasminogen/plasmin system. Thromb Haemost. 2005; 93:647–654. [PubMed: 15841308]
54. Andreasen PA, Egelund R, Petersen HH. The plasminogen activation system in tumor growth, invasion, and metastasis. Cell Mol Life Sci. 2000; 57:25–40. [PubMed: 10949579]
55. Carmeliet P, Moons L, Lijnen R, Baes M, Lemaitre V, Tipping P, Drew A, Eeckhout Y, Shapiro S, Lupu F, Collen D. Urokinase-generated plasmin activates matrix metalloproteinases during aneurysm formation. Nat Genet. 1997; 17:439–444. [PubMed: 9398846]

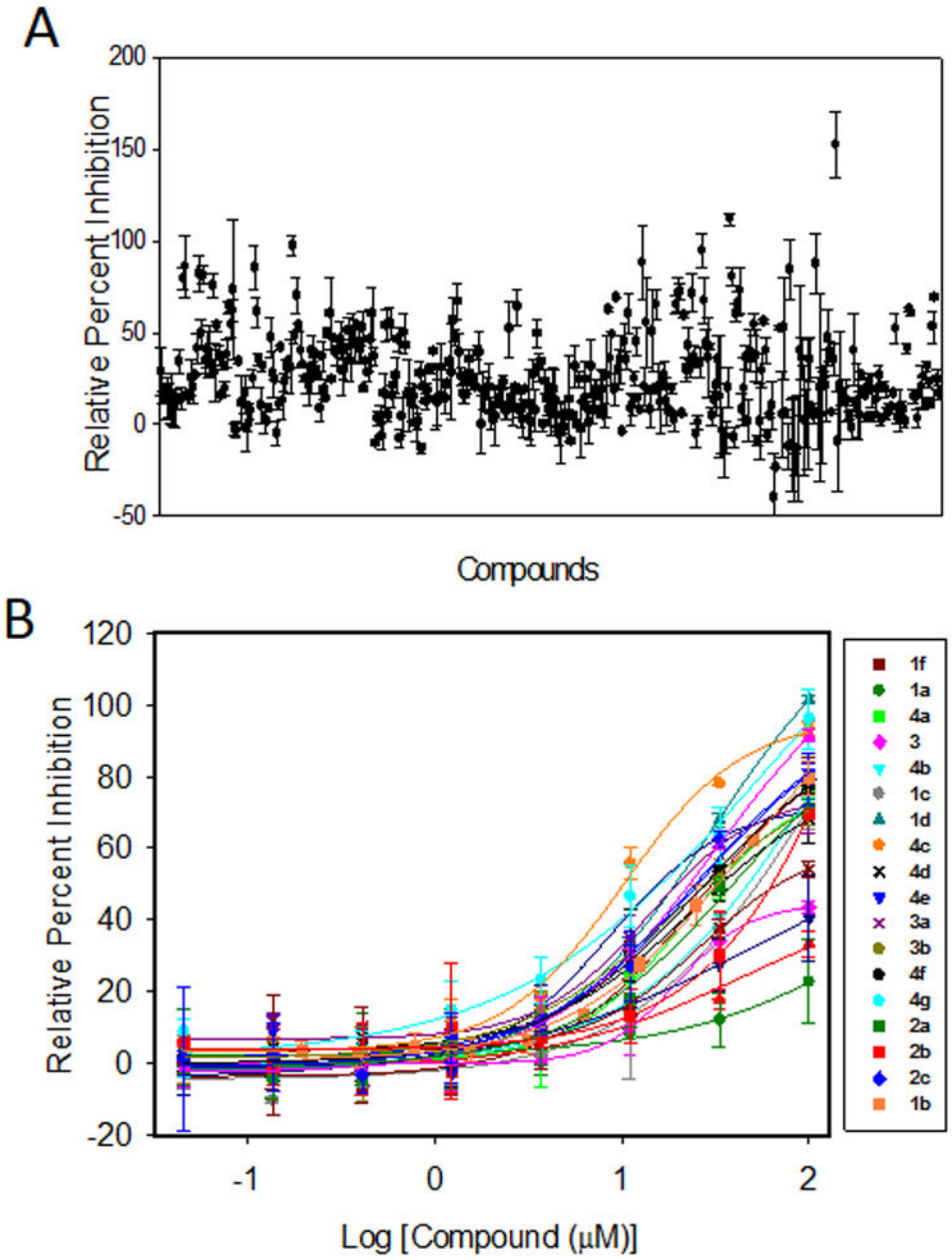


**Figure 1. Fluorescence polarization**

**(A)**Fluorescence polarization screening of 393 compounds that are derivatives of **1-4**. Compounds were screened against uPAR (320 nM) and AE147-FAM peptide (100 nM) at 50 μM. **(B)** Concentration-dependent fluorescence polarization study of the top 22 compounds.

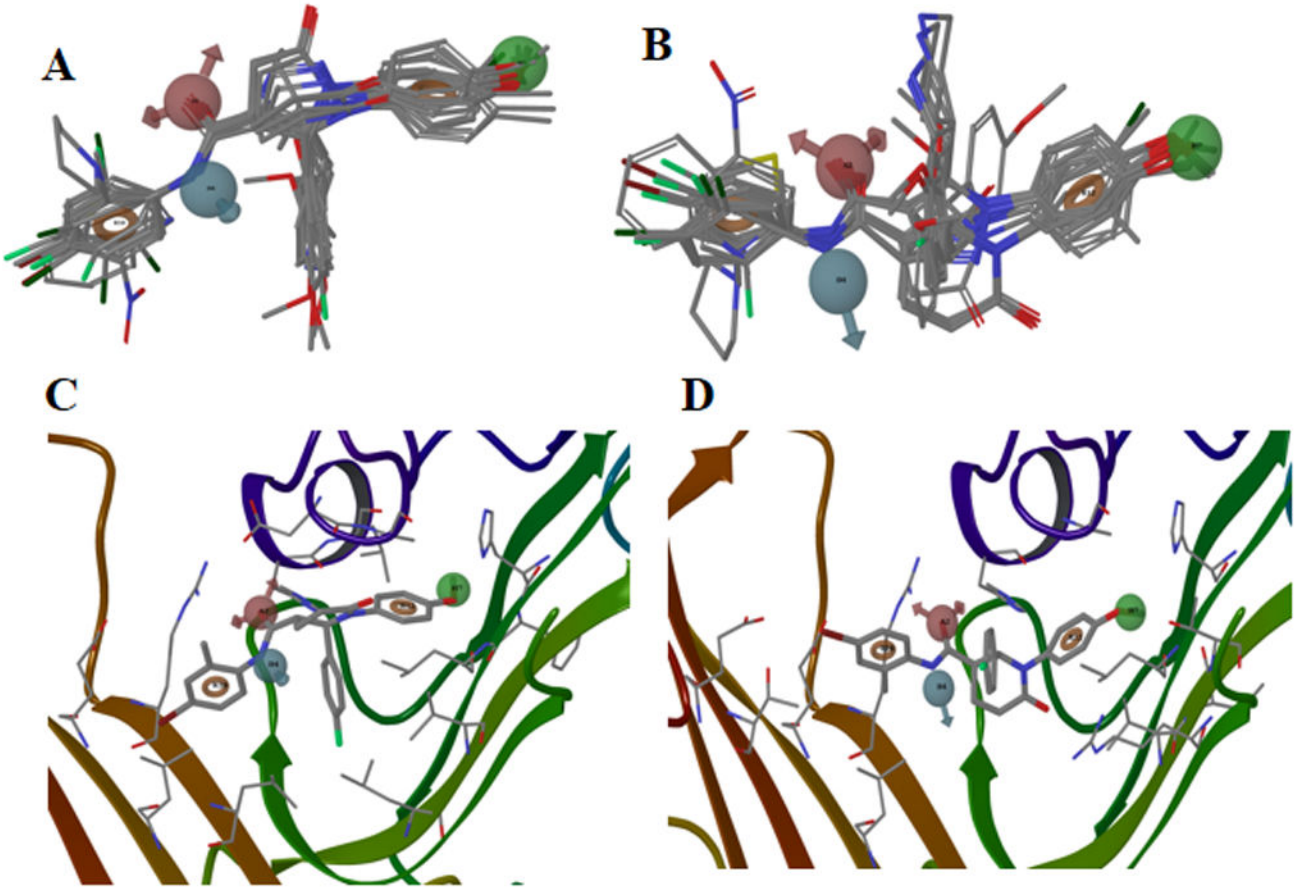


**Figure 2. Compound binding modes**

Hypothesis HS1119 (**A,C**) and HS1135 (**B, D**) that emerged from pharmacophore and QSAR modeling. Features were rendered as orange rings (aromatic ring), green spheres (hydrophobic), blue spheres (donor), and pink spheres (acceptor). All active compounds (shown in sticks) were aligned to pharmacophore hypothesis in **A** and **B**. The pharmacophore along with its reference compound was shown in the pocket of uPAR, which is shown as ribbon (**C,D**). The residues making contact with the reference compound were rendered in thinner capped-sticks.

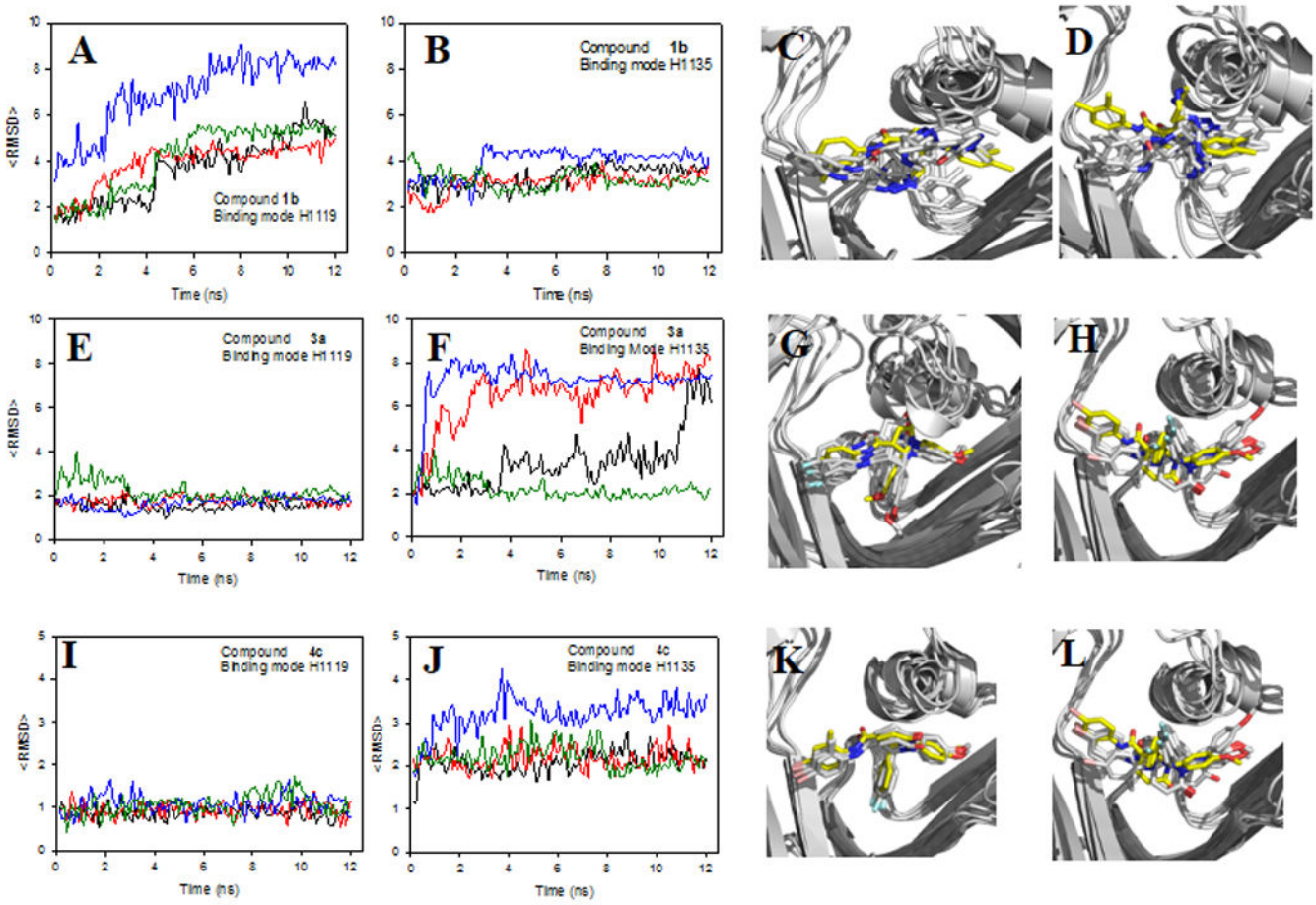


**Figure 3. Compound binding mode stability**

Root-mean-square deviation (RMSD) of compound versus time for **1b** (**A**-**B**), **3a** (**E**-**F**), and **4c** (**I**-**J**), and corresponding illustration of the motion of the compound for **1b** (**C**-**D**), **3a** (**G**-**H**), and **4c** (**K**-**L**). RMSDs are determined for the compound relative to the initial docked structure. Illustrations of superimposed snapshots collected over the course of the trajectories are shown in ribbon representation for uPAR and in capped-sticks for compound (C, N, O, Cl and Br are shown in white, blue, red, pink and cyan, respectively). Carbon atoms are shown in yellow for the initial docked structure.

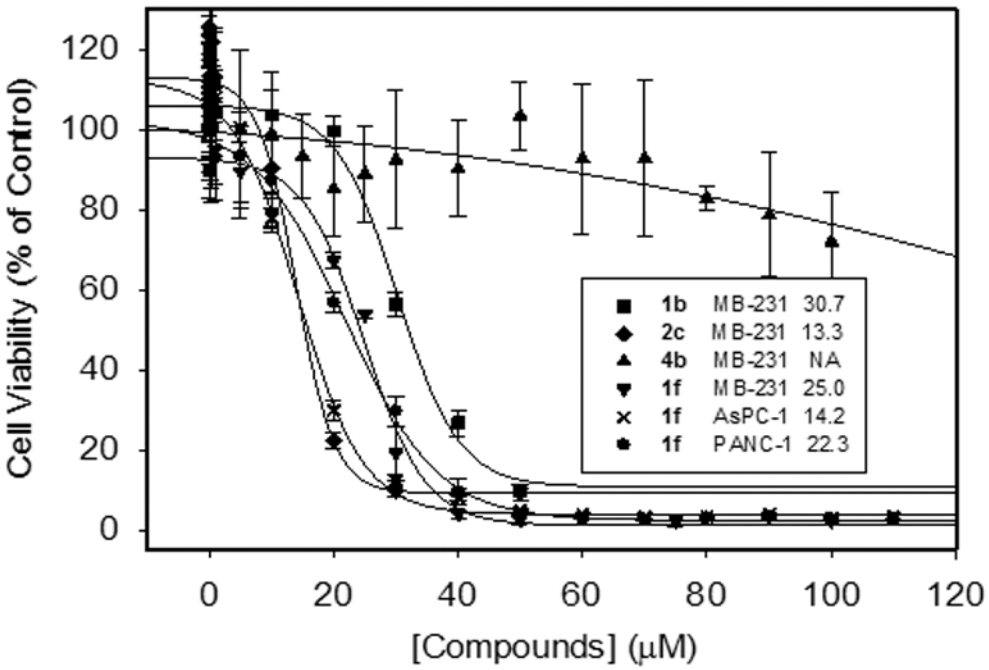


**Figure 4. Cytotoxicity and cell viability studies**

Effects of **1b**, **1f**, **2c**, **4b** on MDA-MB-231, AsPC-1 and PANC-1 cell viability as assessed by MTT assay.

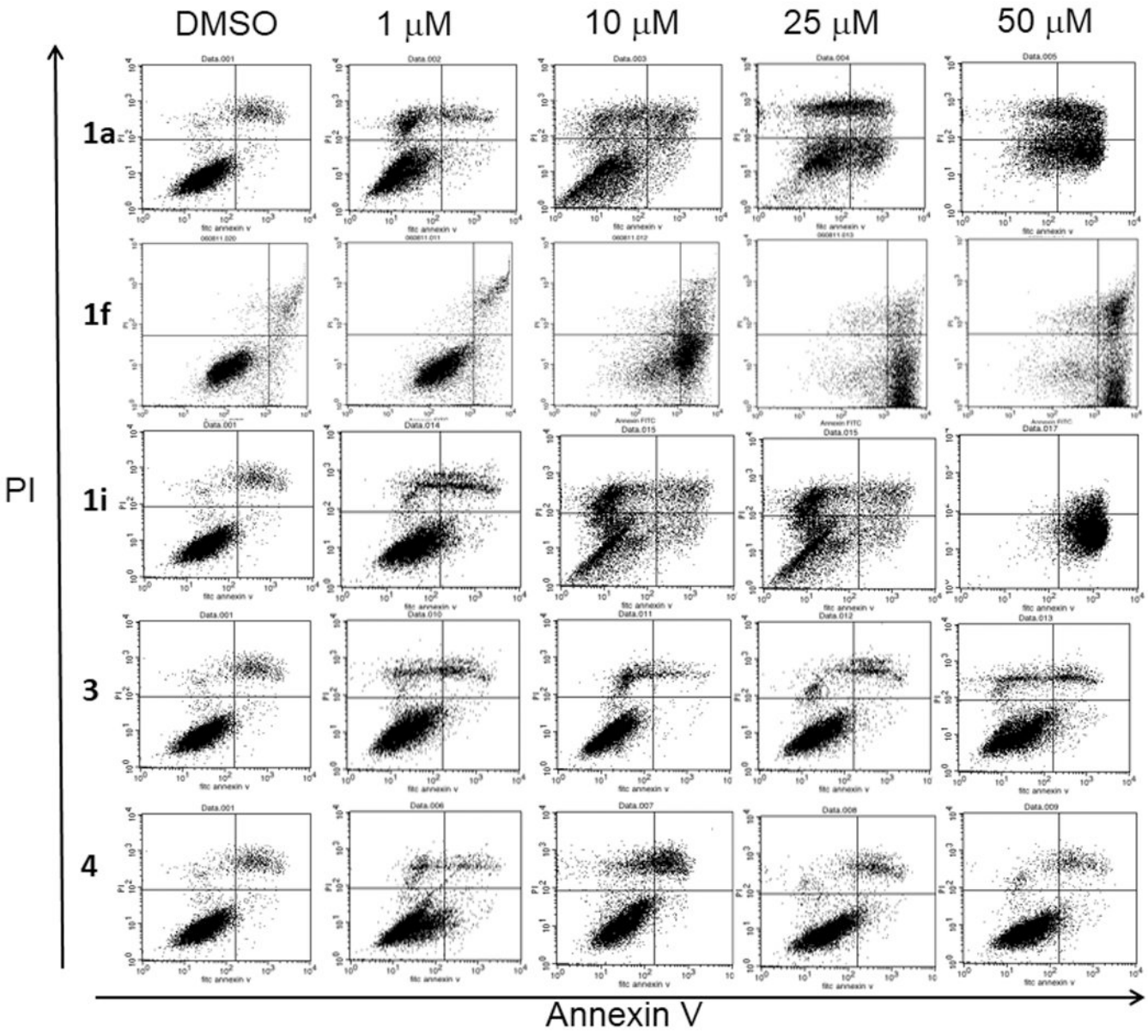


**Figure 5. Flow cytometer analysis using Annexin V-FITC and PI staining**

MDA-MB-231 cells were treated for 24 hr with **1f**, **1a**, **1i**, **3** or **4** and analyzed for apoptosis and necrosis by flow cytometry.

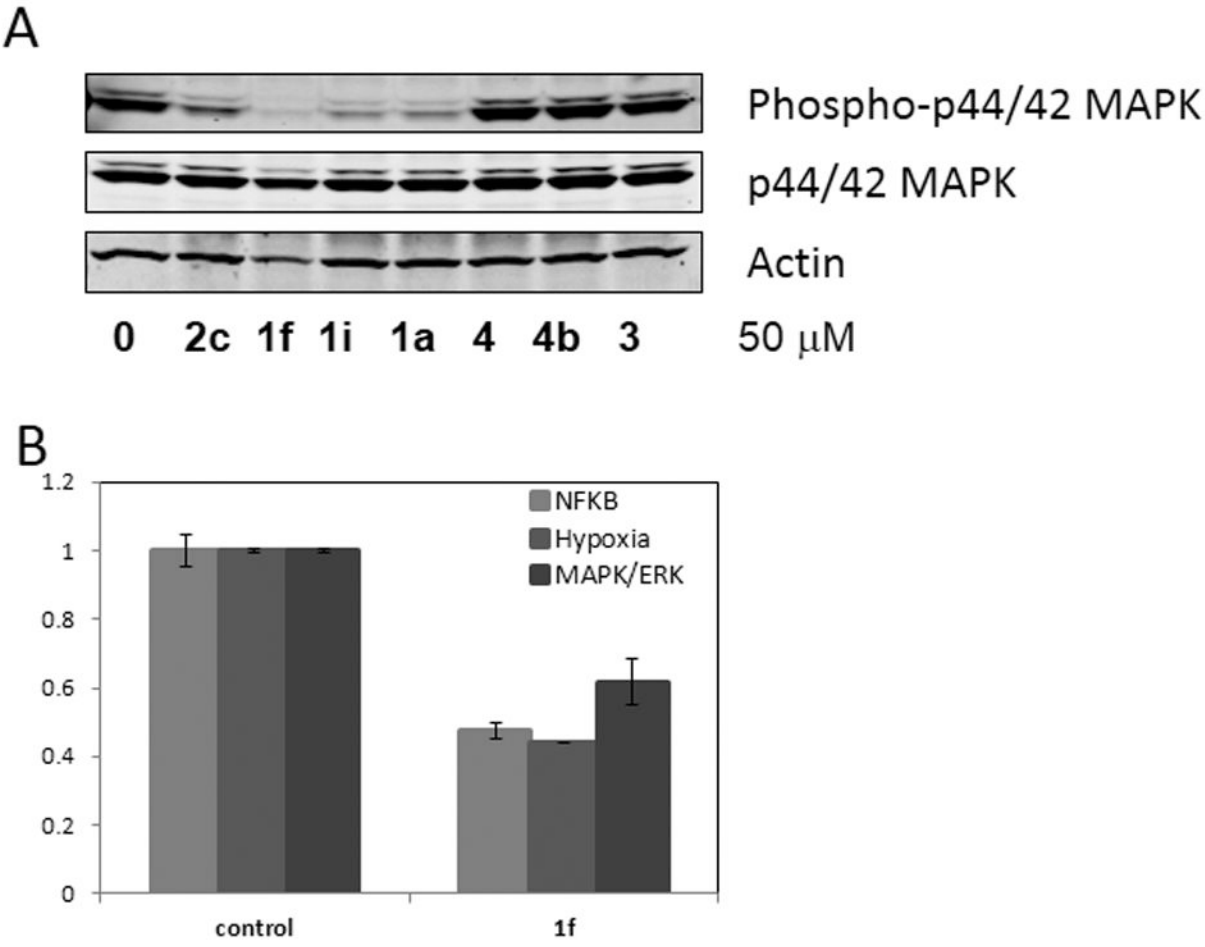


**Figure 6. Effect on signaling**

**(A)**Western immunoblotting showing the effects of compounds at 50 μM concentration on phospho-p44/42 MAPK and total p44/42 MAPK in MDA-MB-231 cell lysates prepared as described in Materials and Methods. Actin is shown as loading control. **(B)** Luciferase reporter assay testing NF-κB, Hypoxia, MAPK/ERK transcription of **1f** on MDA-MB-231 cells.

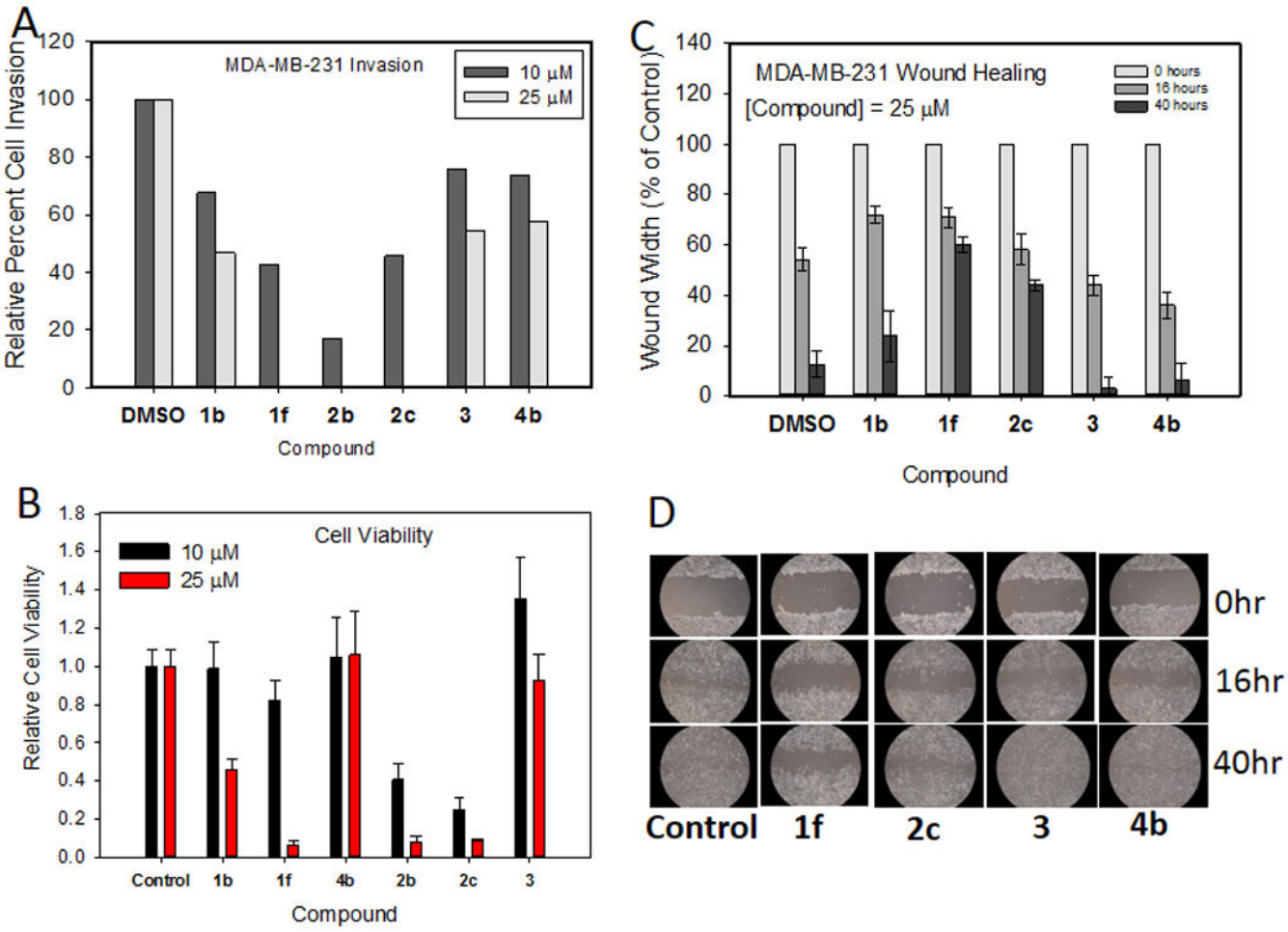


**Figure 7. Invasion and migration studies**

**(A)**Boyden chamber apparatus (with Matrigel) is used to assess the effects of compounds at 10 μM and 25 μM concentrations on MDA-MB-231 invasion. **(B)** Cell viability measured by MTT after 16 hours within the time frame of the invasion studies. **(C)** Effects of compounds at 25 μM concentration on MDA-MB-231 migration as assessed by wound healing assay. **(D)** Snapshots taken over the course of the wound healing experiment to illustrate the effect of the compounds on migration.

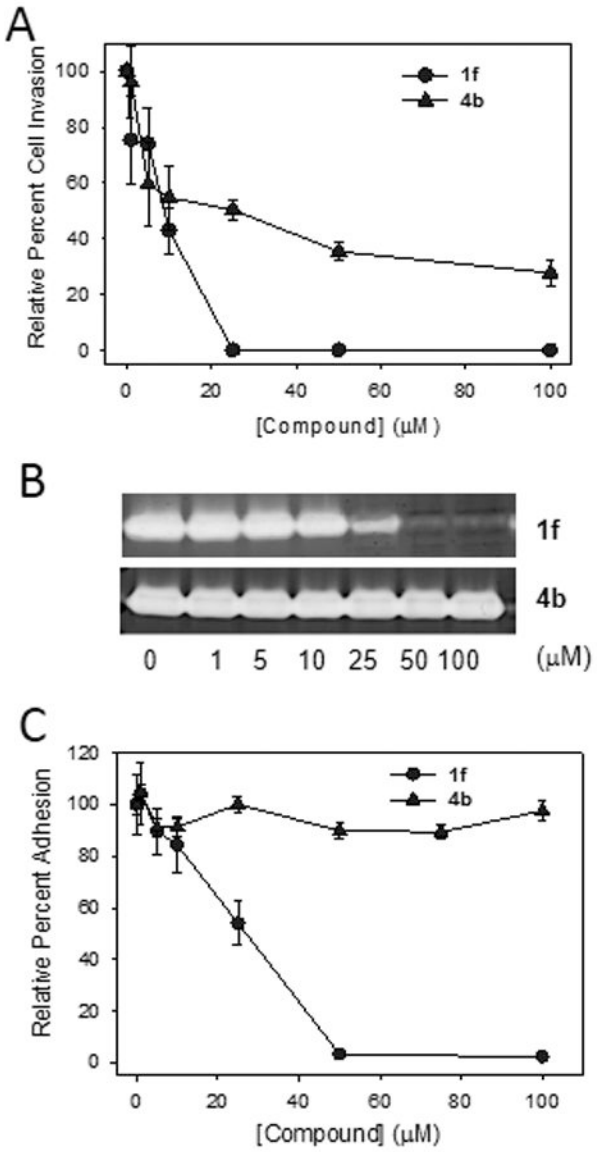


**Figure 8. Invasion, MMP activity and adhesion studies**

**(A)**Boyden chamber apparatus (with Matrigel) is used to assess the effect of **1f** and **4b** on MDA-MB-231 invasion in a concentration dependent manner. **(B)** Effect of **1f** and **4b** on MDA-MB-231 matrix metalloproteinase (MMP-9) activity using gelatin zymography. **(C)** Effect of **1f** and **4b** on MDA-MB-231 cell adhesion to fibronectin.

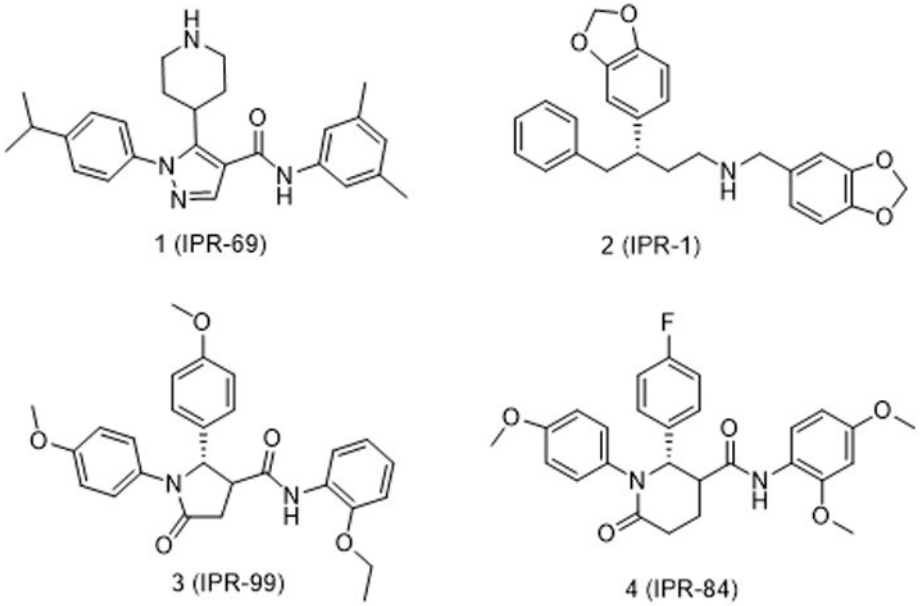


**Scheme 1.**

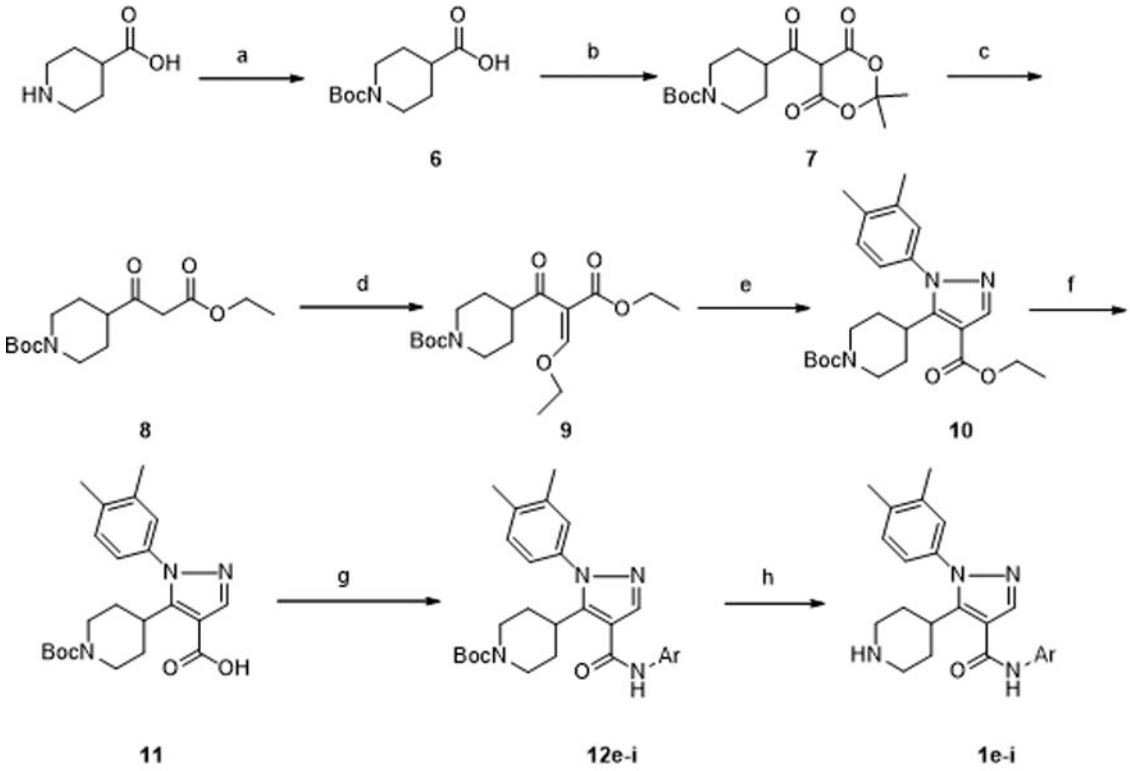


**1e**: Ar = 3-methoxy-5-trifluoromethyl
**1f**: Ar = 2-benzyloxy
**1g**: Ar = 4-fluorophenethyl
**1h**: Ar = 4-isopropyl
**1i**: Ar = 4-propyl

Reagents and Conditions: (a) $K_2CO_3$, di-tert-butyl-di-carbonate, THF:$H_2O$, 0°C. (b) DMAP, DCC, 2,2-dimethyl-1,3-dioxane-4,6-dione, DCM, 0°C. (c) ethanol, reflux. (d) triethylorthoformate, acetic anhydride, reflux. (e) ethanol, hydrazines, reflux. (f) 2.0 M NaOH (aq), ethanol, 70°C. (g) DMAP, DCC, anilines, DCM, 0°C. (h) trifluoroacetic acid:DCM, 0°C.

**Scheme 2.**

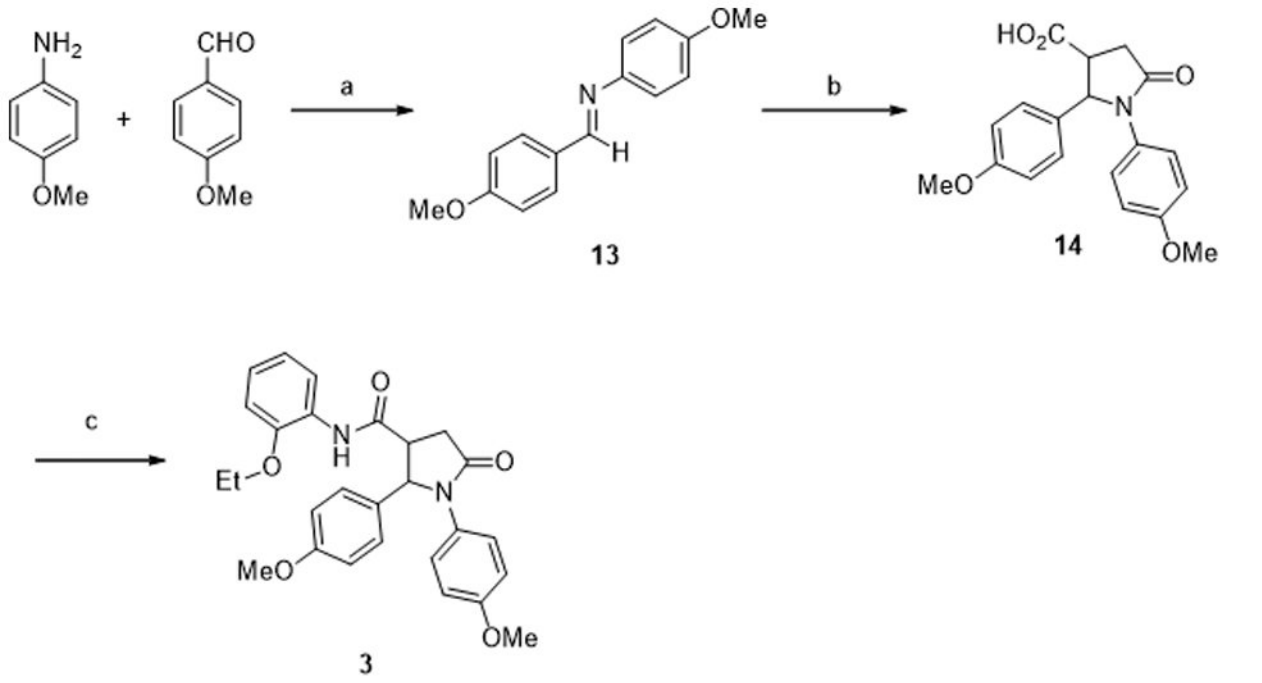


Reagents and Conditions: a) anhydrous $MgSO_4$, DCM, r.t. b) succinic anhydride, xylenes, reflux c) DMAP, DCC, o-phenetidine, DCM, 0°C to r.t.

**Scheme 3.**

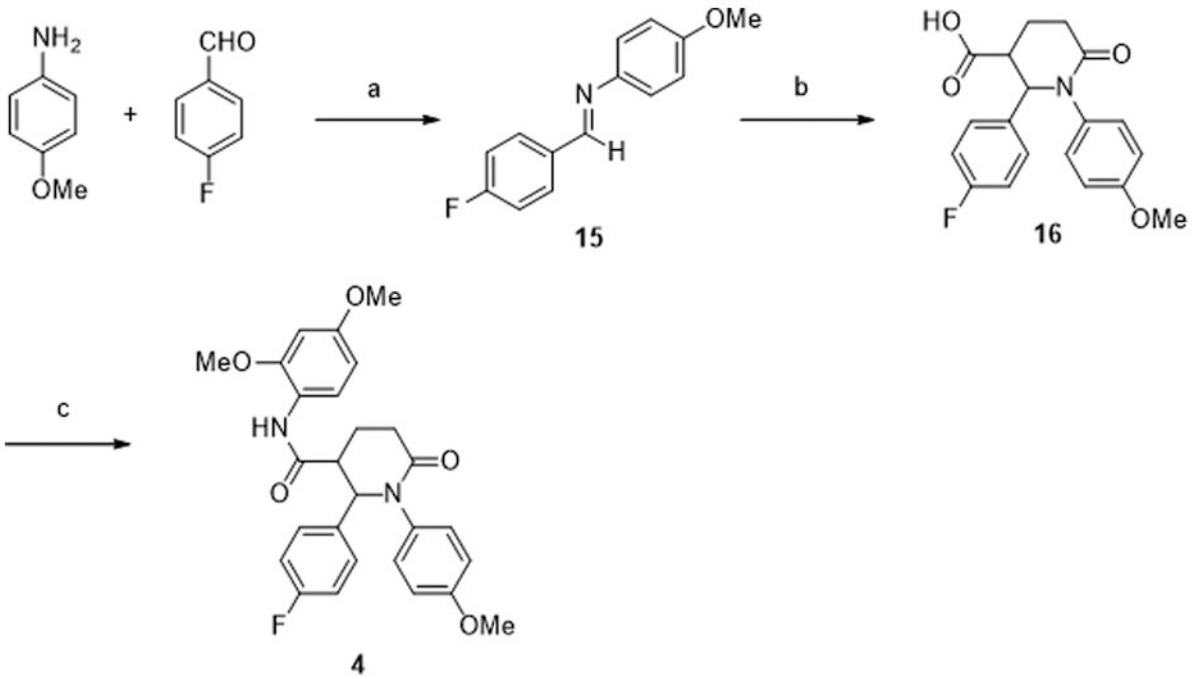


Reagents and Conditions: a) anhydrous $MgSO_4$, DCM, r.t. b) glutaric anhydride, xylenes, reflux c) EDC, HOBT, 2,4-dimethoxyaniline, DCM, 0°C to r.t.

**Scheme 4.**

**Table 1**

**Derivatives of 1**

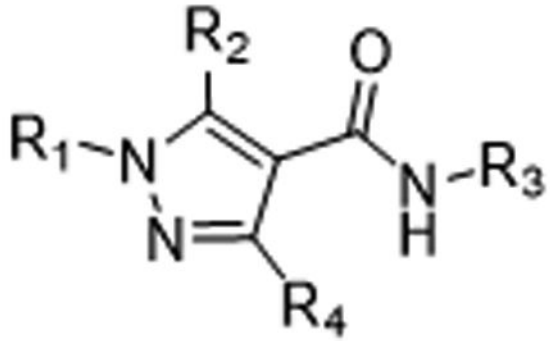


| | $R_1$ | $R_2$ | $R_3$ | $R_4$ | *Ki*(μM) |
|---|---|---|---|---|---|
| **1a**(IPR-81) | 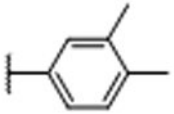 | 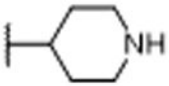 | 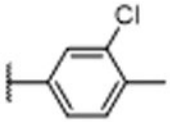 | 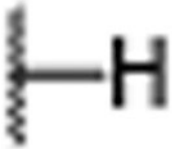 | 21.9 |
| **1b** (IPR-82) | 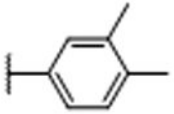 | 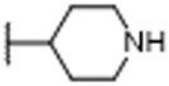 |  | 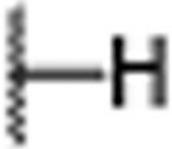 | 18.9 |

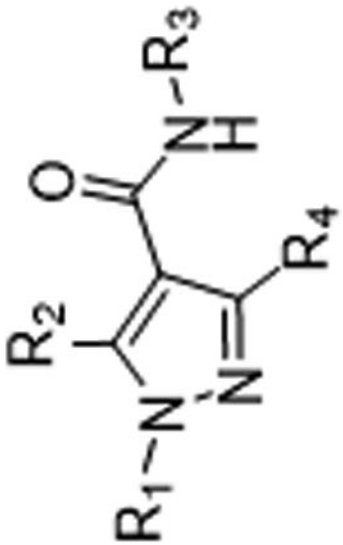

| | $R_1$ | $R_2$ | $R_3$ | $R_4$ | *Ki*(μM) |
|---|---|---|---|---|---|
| **1c**(IPR-361) | 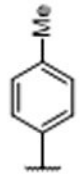 | 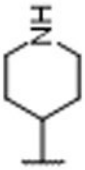 | 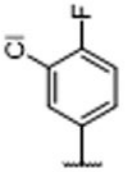 |  | 27.0 |
| **1d** (IPR-380) | 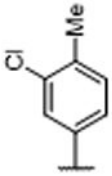 | 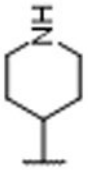 | 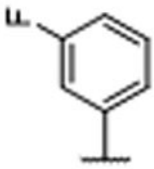 |  | 10.3 |
| **1e**(IPR-735) | 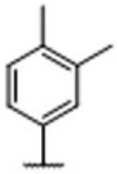 | 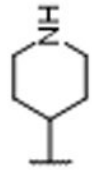 | 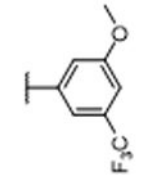 |  | 51.2 |

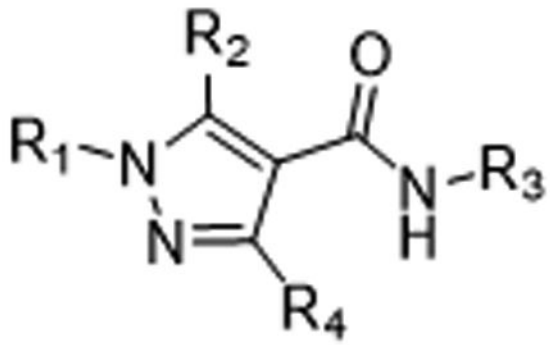


| | $R_1$ | $R_2$ | $R_3$ | $R_4$ | *Ki*(μM) |
|---|---|---|---|---|---|
| **1f**(IPR-737I | 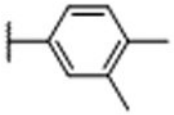 | 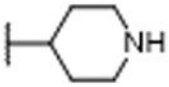 | 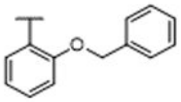 | 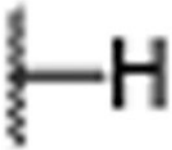 | 17.2 |
| **1g** (IPR-743) | 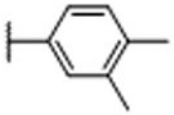 | 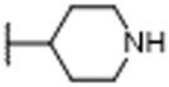 | 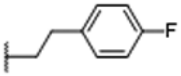 | 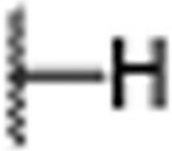 | 28.3 |
| **1h** (IPR-744) | 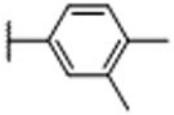 | 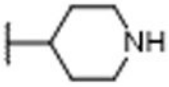 | 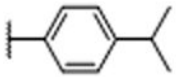 | 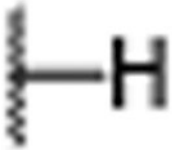 | 63.3 |

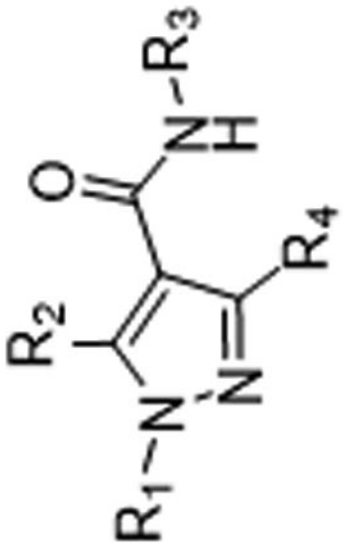

| | $R_1$ | $R_2$ | $R_3$ | $R_4$ | *Ki*(μM) |
|---|---|---|---|---|---|
| **1i** (IPR-745) | 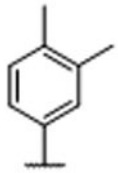 | 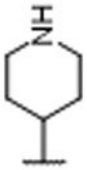 | 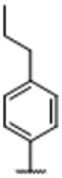 |  | 31.9 |

**Table 2**

**Derivatives of 2**

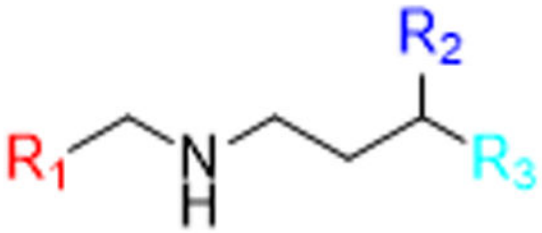


| Compound | $R_1$ | $R_2$ | $R_3$ | *Ki*(μM) |
|---|---|---|---|---|
| **2a** (IPR-8) | 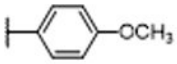 | 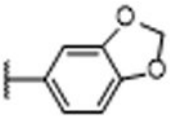 | 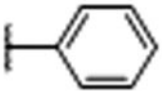 | 19.3 |
| **2b** (IPR-21) | 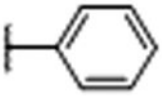 | 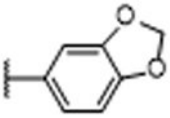 | 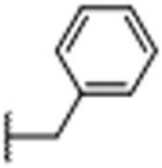 | 33.8 |
| **2c** (IPR-22) | 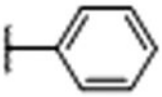 | 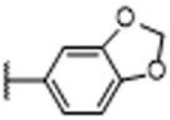 | 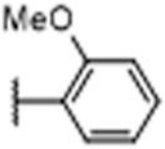 | 13.9 |

**Table 3**

**Derivatives of 3**

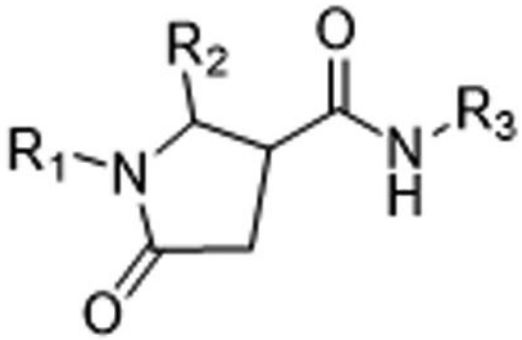


| Compound | $R_1$ | $R_2$ | $R_3$ | $IC_{50}$(μM) | $K_i$(μM) |
|---|---|---|---|---|---|
| **3** (IPR-99) | 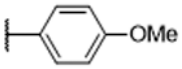 | 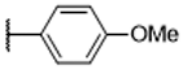 | 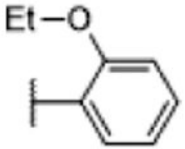 | ND | ND |
| **3a** (IPR-979) | 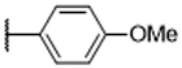 | 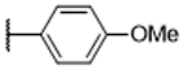 |  | 18 | 10.3 |
| **3b**(IPR-994) | 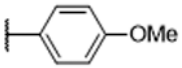 | 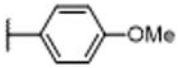 |  | 20 | 11.4 |

**Table 4**

**Derivatives of 4**

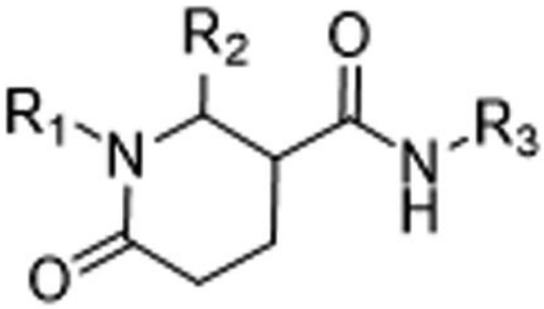


| Compound | $R_1$ | $R_2$ | $R_3$ | *Ki*(μM) |
|---|---|---|---|---|
| **4** (IPR-84) | 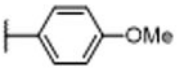 |  | 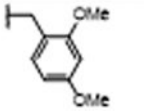 | 18.9 |
| **4a**(IPR-89) | 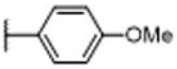 |  | 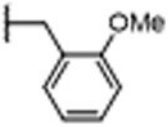 | 18.9 |
| **4b** (IPR-108) | 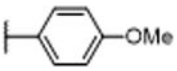 | 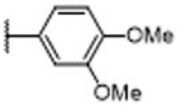 | 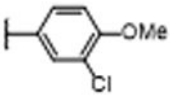 | 24.1 |
| **4c** (IPR-949) | 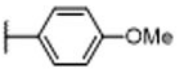 |  | 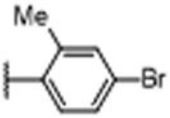 | 5.7 |
| **4d** (IPR-968) | 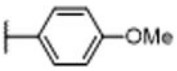 |  | 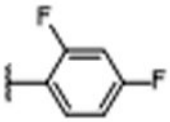 | 19.5 |
| **4e** (IPR-974) | 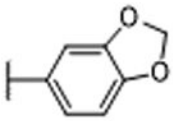 | 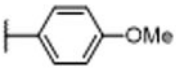 |  | 16.0 |

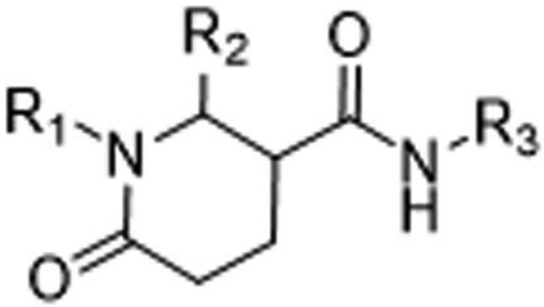


| Compound | $R_1$ | $R_2$ | $R_3$ | *Ki*(μM) |
|---|---|---|---|---|
| **4f** (IPR-1036) | 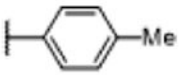 | 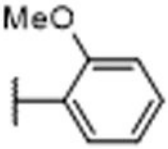 | 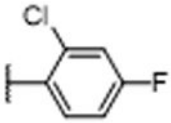 | 12.6 |
| **4g** (IPR-1046) | 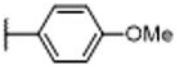 | 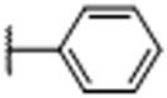 | 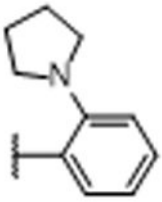 | 10.9 |

## Table 5

**Binding Free Energy and its Components from Computational Studies**

| Compound | Hypothesis | $\Delta E_{VDW}$ | $\Delta E_{PBEIE}$ | $\Delta E_{GBELE}$ | $\Delta E_{SA}$ | $\Delta E_{PBTOT}$ | $\Delta E_{GBTOT}$ | $T\Delta S_{NM}$ | $\Delta G_{PBSA}$ | $\Delta G_{GB}$ |
|---|---|---|---|---|---|---|---|---|---|---|
| **1a** | H1119 | unstable | | | | | | | | |
| | H1135 | -49.3±0.2 | 20.0±0.2 | 18.2±0.1 | -5.6±0.0 | -34.9±0.2 | -36.7±0.2 | -23.4±0.6 | -11.5±0.6 | -13.3±0.6 |
| **3a** | H1119 | -54.2±0.2 | 18.6±0.3 | 18.4±0.1 | -6.9±0.0 | -42.5±0.2 | -42.7±0.2 | -22.4±0.6 | -20.1±0.6 | -20.3±0.6 |
| | H1135 | -43.6±0.2 | 22.1±0.2 | 18.9±0.1 | -6.2±0.0 | -27.7±0.2 | -30.9±0.2 | -19.9±0.6 | -7.8±0.6 | -11.0±0.6 |
| **4c** | H1119 | -55.7±0.1 | 15.0±0.2 | 15.3±0.1 | -6.6±0.0 | -47.4±0.2 | -47.0±0.2 | -22.0±0.6 | -25.4±0.6 | -25.0±0.6 |
| | H1135 | -53.8±0.1 | 17.4±0.1 | 15.6±0.1 | -6.6±0.0 | -43.0±0.2 | -44.8±0.2 | -23.5±0.6 | -19.5±0.6 | -21.3±0.6 |

$\Delta E_{VDW}$, van der Waals potential energy; $\Delta E_{PBEIE}$, electrostatic contributions to the binding energy, of which the polar solvent contributions were calculated with Poisson-Boltzmann equation; $\Delta E_{GBELE}$, electrostatic contributions to the binding energy, of which the polar solvent contributions were calculated with Generalized Born equation; $\Delta E_{SA}$, nonpolar solvent contribution to solvation free energy; $\Delta E_{PBTOT}$, the sum of $\Delta E_{VDW}$, $\Delta EI_{PBELE}$ and $\Delta E_{SA}$; $\Delta E_{GBTOT}$, the sum of $\Delta E_{VDW}$, $\Delta E_{GBELE}$ and $\Delta E_{SA}$; $T\Delta S_{NM}$, entropy calculated with normal mode analysis; $\Delta G_{PB}$, the calculated free energy of binding using PB model; $\Delta G_{GB}$, the calculated free energy of binding using GB model.

## Table 6

**Mechanism of Compound Cell Killing Studied by Flow Cytometry**

| | | DMSO | 1 μM | 10 μM | 25 μM | 50 μM |
|---|---|---|---|---|---|---|
| **1a** | Percentage apoptosis | 2 | 1 | 5 | 16 | 39 |
| | Percentage necrosis | 6 | 5 | 12 | 17 | 32 |
| **1f** | Percentage apoptosis | 3 | 3 | 45 | 76 | 61 |
| | Percentage necrosis | 6 | 7 | 15 | 8 | 21 |
| **1i** | Percentage apoptosis | 2 | 11 | 6 | 46 | 86 |
| | Percentage necrosis | 6 | 7 | 9 | 10 | 12 |
| **3** | Percentage apoptosis | 2 | 2 | 1 | 2 | 4 |
| | Percentage necrosis | 6 | 6 | 3 | 8 | 7 |
| **4** | Percentage apoptosis | 2 | 4 | 2 | 3 | 3 |
| | Percentage necrosis | 6 | 3 | 14 | 6 | 5 |